3D wave-resolving simulation of sandbar migration

Patrick Marchesiello, Julien Chauchat, Hassan Shafiei, Rafael Almar, Rachid Benshila, Franck Dumas, Laurent Debreu

3D wave-resolving simulation of sandbar migration

Patrick Marchesiello[a,*], Julien Chauchat[b], Hassan Shafiei[b], Rafael Almar[a], Rachid Benshila[c], Franck Dumas[d], Laurent Debreu[e]

[a] *IRD/LEGOS, Toulouse, France*
[b] *Univ. Grenoble Alpes, CNRS, Grenoble INP, LEGI, 38000 Grenoble, France*
[c] *CNRS/LEGOS, Toulouse, France*
[d] *SHOM, Brest, France*
[e] *Univ. Grenoble Alpes, Inria, CNRS, Grenoble INP, LJK, 38000 Grenoble, France*

Abstract

The problem of sandbar migration on the storm timescale is revisited with a 3D wave-resolving hydro-sedimentary model. The latter presents an intermediate approach between expensive wave-resolving two-phase flow models and highly parametrized wave-averaged models. Innovative features include the use of weakly compressible assumptions in the hydrodynamics and morphological acceleration of bed changes to speed up numerical simulations. The model accurately simulates the successive offshore and onshore bar migration observed in a large-scale flume experiment in response to wave forcing representing storm and post-storm (recovery) conditions. The diagnosis of sand transport and the analysis of an ensemble-averaged asymmetric wave cycle reveal the migration mechanisms in each phase. In all cases, sediment resuspension is impacted by breaker-induced turbulence, while sediment transport and bed evolution are primarily the result of the undertow distribution — the breaker-induced seaward undercurrent — across the sandbar. There is also a significant contribution from asymmetric wave-related onshore fluxes, due to greater mobilization and currents during the wave crest period.

Keywords: nearshore, sandbar migration, wave-resolving model, wave asymmetry, sediment transport

*Corresponding author
Email address: patrick.marchesiello@ird.fr (Patrick Marchesiello)

1. Introduction

The presence of nearshore sandbars are ubiquitous on natural beaches, which are prime areas for morphological changes, depending on wave and sediment characteristics (Roelvink and Stive, 1989; Thornton et al., 1996; Elgar et al., 2001; Almar et al., 2010; Grasso et al., 2011). However, they present a challenge to our understanding of sediment transport processes, which is often based on the study of non-breaking waves (Scott et al., 2009; van der Zanden et al., 2017; Lim et al., 2020). Numerical modeling can often be used to study these processes in a timely and cost-effective manner, but it typically relies on many assumptions and unknown parameters, so many aspects of bar dynamics remain unclear (Roelvink et al., 2012).

In particular, the role of wave asymmetry on bar migration is actively debated (Grasso et al., 2011). Velocity skewness (sharp, high crests and broad, shallow troughs) and asymmetry (saw tooth-type waves) are considered to be responsible for sediment transport in the direction of wave propagation (onshore). The basic idea is that fast crest velocities in the onshore direction would mobilize and transport more sediment than the offshore-directed trough velocities (Hsu and Hanes, 2004). Wave asymmetry with its steep front would more efficiently mobilize sediments than skewness (Drake and Calantoni, 2001), possibly also reducing the phase lag between mobilization and transport (Dohmen-Janssen et al., 2002). Breaking waves may also contribute to bed shear stress and thus mobilization asymmetry due to higher turbulence intensity during the wave crest period (Ting and Kirby, 1994), although this process is disputed (Scott et al., 2009). In addition, in contrast to the surface elevation, the low-frequency components of the orbital velocity (subharmonics) can contribute to a negative subsurface skewness in the most energetic wave groups (Alberello et al., 2016). Interestingly, it is generally assumed that bar migration results from a trade-off between onshore and offshore fluxes (e.g., Grasso et al. 2011), thus confusing the notions of convergent and confluent fluxes. A comprehensive conceptual model that could describe the interaction between onshore and offshore transport processes in bar migration, allowing for variable wave forcing, is still needed. The present work is a step in that direction.

It will confirm the existence of wave-related onshore transport (especially in the accretion phase) but will show that sediment transport around the sandbar depends primarily on the cross-shore distribution of the undertow, which varies with wave height.

Two-phase (water and sediment) flow models applied to individual wave breaking can be used to describe the hydro-morphodynamics in great detail (Cheng et al., 2017; Kim et al., 2019). This approach does not require parameterization of sand resuspension or solving the Exner equation for bed evolution, but it does require grid resolution on the order of grain size, and constitutive laws for particle-particle and fluid-particle interactions. As a result, these models are theoretically difficult, algorithmically complex, and computationally very expensive (Chauchat et al., 2017). Therefore, the study of sandbar formation and migration has been done in the past with much simpler depth-averaged and/or wave-averaged models (Watanabe, 1982; Stive, 1986; Roelvink and Stive, 1989; van Rijn et al., 2003; Long et al.), which are used operationally today — XBeach being a classic example (Rafati et al., 2021). These models rely heavily on parametrizations to account for both onshore and offshore sandbar migration, i.e., a balance between offshore transport by the undertow and onshore transport by skewed/asymmetric waves and wave streaming. Depth-dependent phase-averaged nearshore models (McWilliams et al., 2004) have improved the representation of the undertow, but the effects of wave asymmetry/skewness remain parametrized as bedload transport in the wave boundary layer (e.g., van der Werf et al. 2015 for Delft3D; Kalra et al. 2019 for ROMS; Shafiei et al. 2022 for CROCO). Recently, empirical formulations have improved, using the concept of half-wave cycles (Dibajnia and Watanabe, 1992; van der A et al., 2013), and are implemented with mixed success (Veen, 2014; Schnitzler, 2015).

As an intermediate approach between expensive wave-resolving two-phase flow models and highly parametrized wave-averaged models, we propose to apply a wave-resolving, free-surface, coupled hydro-sedimentary model. CROCO (Coastal and Regional Ocean Community model) has recently been adapted to nearshore wave dynamics and circulation problems (Marchesiello et al., 2021). This cost-effective 3D wave-resolving model can explicitly simulated the vertical profiles of oscillatory cross-shore sediment transport, allowing assessment

of the combined effects of mean undertow and asymmetric waves around a sandbar. This paper presents a brief overview of the CROCO coupled hydro-sedimentary model, before discussing its application to a large-scale flume experiment (LIP11D), and an analysis of offshore and onshore sandbar migration under wave forcing representing storm and post-storm (recovery) conditions.

2. Model description

The development of 3D wave-resolving models to study nearshore dynamics in realistic environments has been limited by computing resources and the cost-effective use of these resources. Early applications starting in the 1990s used the volume-of-fluid (VOF) method for free-surface tracking (e.g., Lin and Liu 1998; Watanabe and Saeki 1999; Derakhti and Kirby 2014; Larsen et al. 2020). This model type with Cartesian coordinate, where the free surface crosses computational cells arbitrarily, is computationally intensive and does not allow the pressure boundary condition to be precisely applied on the free surface, which affects the overall accuracy of the model (Chen et al., 2018). More recently, several 3D wave-resolving, free-surface and terrain-following models based on Reynolds-Averaged Navier-Stokes (RANS) equations have emerged for the nearshore zone, e.g., SWASH (Zijlema et al., 2011), NHWAVE (Derakhti et al., 2016), and CROCO (Marchesiello et al., 2021). In this case, the explicit overturning of the free surface is excluded and the breaking wave is modeled with a single-valued free surface which follows a shock process and resembles a dissipating bore. Despite the absence of explicit overturning (replaced by parametrized turbulence), these models can be accurate as well as computationally efficient (orders of magnitude cheaper) in the study of waves and wave-driven mean and transient circulation.

CROCO (`www.croco-ocean.org`) belongs to this class of models but, contrary to the other attempts, it solves the compressible Navier-Stokes equations (Auclair et al., 2018). A compressible approach preserves the hyperbolic nature of Navier-Stokes equations and does not require a global elliptic solver with incremental pressure corrections to ensure the incompressible mass balance. As a result, it avoids splitting errors between pressure and velocity and approximations made on free-surface conditions (Zijlema et al., 2011; Derakhti

et al., 2016), thereby preserving amplitude and nonlinear dispersive properties of surface waves. In the same time, the absence of global computations by an elliptic solver makes optimization and parallelization procedures much more efficient (excellent scalability even on massively parallel computers). The cost of solving acoustic waves is managed with a time-splitting technique and semi-implicit time discretization.

2.1. Model equations

The full set of Navier-Stokes equations for a free-surface ocean model is explicitly integrated in the nonhydrostatic, non-Boussinesq (compressible) version of CROCO, built on the code structure of ROMS primitive equation solver (Shchepetkin and McWilliams, 2005; Debreu et al., 2012). Non-Boussinesq equations include the momentum and continuity equations, the free-surface kinematic condition, conservation equations for heat, salt or other tracer C (such as sediment concentration), which reads in Cartesian coordinates:

$$\frac{\partial \rho u}{\partial t} = -\vec{\nabla}.\left(\rho \vec{\mathbf{v}} u\right) + \rho f v - \rho \tilde{f} w - \frac{\partial P}{\partial x} + \mathcal{F}_u + \mathcal{D}_u \tag{1}$$

$$\frac{\partial \rho v}{\partial t} = -\vec{\nabla}.\left(\rho \vec{\mathbf{v}} v\right) - \rho f u - \frac{\partial P}{\partial y} + \mathcal{F}_v + \mathcal{D}_v \tag{2}$$

$$\frac{\partial \rho w}{\partial t} = -\vec{\nabla}.\left(\rho \vec{\mathbf{v}} w\right) + \rho \tilde{f} u - \frac{\partial P}{\partial z} - \rho g + \mathcal{F}_w + \mathcal{D}_w \tag{3}$$

$$\frac{\partial \rho}{\partial t} = -\vec{\nabla}.(\rho \vec{\mathbf{v}}) \tag{4}$$

$$\frac{\partial \eta}{\partial t} = \left. w\right|_{z=\eta} - \left.\vec{\mathbf{v}}\right|_{z=\eta}.\vec{\nabla}\eta \tag{5}$$

$$\frac{\partial \rho C}{\partial t} = -\vec{\nabla}.(\rho \vec{\mathbf{v}} C) + \mathcal{F}_C + \mathcal{D}_C \tag{6}$$

(u, v, w) are the Cartesian (x,y,z) components of vector velocity $\vec{\mathbf{v}}$; η is the free surface; P the total pressure; ρ the density; $f(x, y)$ and $\tilde{f}(x, y)$ are the traditional and non-traditional

Coriolis parameters, function of latitude; g is acceleration of gravity; $\mathcal{D}_u, \mathcal{D}_v, \mathcal{D}_C$ are eddy-diffusion terms requiring second-moment turbulence closure models (bulk viscosity terms for acoustic wave damping are not used here); $\mathcal{F}_u, \mathcal{F}_v, \mathcal{F}_C$ are forcing terms.

In this study, movements are produced along a channel by a wave generator in a homogeneous non-rotating fluid. In this case, the longitudinal flow equation v disappears and the Coriolis force, the baroclinic pressure force, and all surface fluxes (forcing terms) are zero. There is no temperature or salinity stratification so that the associated density is constant in time and space (but not the dynamic density associated with acoustic waves). The resulting equations are:

$$\frac{\partial \rho u}{\partial t} = -\vec{\nabla}.\left(\rho \vec{\mathbf{v}} u\right) - \frac{\partial P}{\partial x} + \mathcal{D}_u \tag{7}$$

$$\frac{\partial \rho w}{\partial t} = -\vec{\nabla}.\left(\rho \vec{\mathbf{v}} w\right) - \frac{\partial P}{\partial z} - \rho g + \mathcal{D}_w \tag{8}$$

$$\frac{\partial \rho}{\partial t} = -\vec{\nabla}.(\rho \vec{\mathbf{v}}) \tag{9}$$

$$\frac{\partial \eta}{\partial t} = \left. w\right|_{z=\eta} - \left.\vec{\mathbf{v}}\right|_{z=\eta}.\vec{\nabla}\eta \tag{10}$$

$$\frac{\partial \rho C}{\partial t} = -\vec{\nabla}.(\rho \vec{\mathbf{v}} C) + \mathcal{D}_C \tag{11}$$

2.2. Computational procedure

In the above set of equations, a relation between ρ and P is required. To that end, and as part of a time-splitting approach, density is decomposed into a slow component and a fast component based on a first-order linear decomposition with respect to total pressure. The Navier-Stokes equations are then integrated with two different time steps within the time-splitting approach inherited from ROMS. The slow mode integration includes the slow part of the vertical momentum equation, while the fast mode integration is in 3D and includes

the compressible terms of the momentum and continuity equations. More details can be found in Appendix A.

Note that acoustic waves can become pseudo-acoustic if their phase speed $c_s = \sqrt{\frac{\partial P}{\partial \rho}}$ is artificially reduced (but not lower than the speed of the shallow water phase). In this case, high-frequency processes associated with bulk compressibility (acoustic waves) may be degraded, but an accurate solution for slower nonhydrostatic dynamics (gravity waves) can be preserved, while relaxing CFL constraints. In our nearshore applications, a c_s value of 100 m/s instead of 1500 m/s makes no difference for the physical solution but allows a great reduction in the computational time (by half).

CROCO is discretized on a C-grid with finite-difference methods for slow and fast modes (Shchepetkin and McWilliams, 2005; Soufflet et al., 2016). In short, the slow-mode time-stepping algorithm is a Leapfrog Adams-Moulton predictor-corrector scheme, that is third-order accurate for integrating advective terms. The fast mode is integrated with a horizontally explicit vertically implicit (HEVI) scheme, i.e. a generalized forward-backward scheme on the horizontal and a backward Euler scheme on the vertical. The implicit backward Euler method solves the terms responsible for vertical acoustic propagation (the terms of the fast mode w equation). It allows for an extended stability range and, since it is a diffusive scheme, it has a damping effect on the acoustic waves, while preserving the gravity waves (Klemp et al., 2018).

The spatial discretization of the horizontal and vertical advection terms uses the improved WENO5-Z version of the 5th-order weighted essentially non-oscillatory scheme (Borges et al., 2008), which is popular for hyperbolic problems containing both shocks and smooth structures. WENO5-Z naturally copes with dispersive numerical modes as well as shocks caused by breaking waves, with no need for *ad hoc* criteria.

2.3. Turbulence closure

Along with the numerical treatment of breaking waves, a k-ϵ or k-ω model, solving the closure equations for turbulent kinetic energy k and dissipation ϵ or dissipation rate $\omega \propto \epsilon\, k^{-1}$, is used as part of a Generic Length Scale (GLS) method (Warner et al., 2005).

In the absence of buoyancy forcing, the turbulence equations express a balance between transport, diffusion, shear production and dissipation:

$$\frac{\partial \rho k}{\partial t} = -\vec{\nabla}.(\rho \vec{\mathbf{v}}\, k) + \mathcal{D}_k + \rho(P - \epsilon) \tag{12}$$

$$\frac{\partial \rho \epsilon}{\partial t} = -\vec{\nabla}.(\rho \vec{\mathbf{v}}\, \epsilon) + \mathcal{D}_\epsilon + \rho \frac{\epsilon}{k}(c_{\epsilon 1} P - c_{\epsilon 2}\epsilon) \tag{13}$$

or

$$\frac{\partial \rho \omega}{\partial t} = -\vec{\nabla}.(\rho \vec{\mathbf{v}}\, \omega) + \mathcal{D}_\omega + \rho \frac{\omega}{k}(c_{\omega 1} P - c_{\omega 2}\epsilon) \tag{14}$$

The eddy viscosity $\nu_t = c_\mu\, l\, k^{\frac{1}{2}}$ is derived from these equations, with coefficient c_μ dependent on stability functions, and mixing length $l \propto k^{\frac{3}{2}}\epsilon^{-1}$. l is resolution independent, which is consistent with a RANS rather than LES approach. The shear production term for k is $P = 2\nu_t S_{ij} S_{ij}$, with the mean strain rate tensor $S_{ij} = \frac{1}{2}(\frac{\partial u_i}{\partial x_j} + \frac{\partial u_j}{\partial x_i})$ (using Einstein notation). All turbulence model parameters are given in Warner et al. (2005), based on Burchard et al. (1998) for k-ϵ and Wilcox (1988) for k-ω. The only present modification concerns the surface and bottom mixing lengths, which are model boundary conditions given by: $l_s = \kappa z_{0s}$ and $l_b = \kappa z_{0b}$. We found that a relatively high value of z_{0b} (5 cm) is needed to match the observed sand concentration profiles near the bottom. With the k-ϵ model, the momentum mixing is also sensitive to z_{0s}, which needs to be increased to 0.2 m in order to match the observed velocity profiles (see validation section 3.3). For this reason, and for its robustness through resolutions, the k-ω model will be our standard turbulence model.

2.4. Wave maker at offshore boundary

The wave maker forces a spectrum of linear waves at the offshore boundary, as in Zijlema et al. (2011). In full 3D applications, the spectrum has frequency and directional spreading Marchesiello et al. (2021) but in this flume experiment, waves are shore normal:

$$\eta_{bc}(t) = \sum_i a_i\, \cos(\omega_i\, t + \phi_i) \tag{15}$$

$$u_{bc}(z,t) = \sum_i a_i\, \omega_i\, \frac{\cosh(k_i(z+h))}{\sinh(k_i h)}\, \cos(\omega_i\, t + \phi_i) \tag{16}$$

where (x,y,z) are cross-shore, alongshore and vertical directions respectively; (i) is the index of spectral distribution; a_i is the amplitude at each frequency ω_i, from a given statistical distribution, e.g., JONSWAP (Sec. 3.2); ω_i and k_i are related by the linear dispersion relation: $\omega_i^2 = g\,k_i\,\tanh(k_i h)$ with h the water depth; ϕ_i is a uniformly distributed random phase.

w_{bc} is set to zero and our tests show only weak sensitivity to this choice. Depth-averaged (barotropic) velocities $(\bar{u}, \bar{v})$ must be provided as well in the wave maker because they are prognostic variables, advanced together with the fast acoustic mode. Normal depth-averaged velocity $\bar{u}$ is complemented at the boundary by an anti-Stokes "compensation flow", opposite to Stokes drift and thus closing the volume budget. We do not impose the depth-averaged value of u_{bc} directly but through the incoming characteristic of the shallow water system as in Flather-type conditions (Marchesiello et al., 2001; Blayo and Debreu, 2005):

$$\bar{u} = \bar{u}_{bc} - \sqrt{\frac{g}{h}}(\eta - \eta_{bc}) \tag{17}$$

This allows infragravity waves generated inside the domain to propagate out as long waves, while ensuring a near conservation of mass and energy through the open boundary. Likewise, the baroclinic components (u_{bc}, w_{bc}) are applied via an adaptive radiation condition which helps short waves and 3D flow perturbations to leave the domain with only a small effect on the interior solution (Marchesiello et al., 2001).

2.5. Sediment transport model

CROCO comes with capabilities for water quality, marine ecosystem and sediment modeling. They are built upon Eq. 6 for the transport of tracer concentration but, in the case of sediment modeling, additional sources and sinks are needed to simulate the exchange between the water column and sediment bed (Blaas et al., 2007; Warner et al., 2008). Neglecting compressibility ($\rho \sim \rho_0$), the sediment concentration follows:

$$\underbrace{\frac{\partial C}{\partial t}}_{RATE} = -\underbrace{\vec{\nabla}.\vec{\mathbf{v}}C}_{ADVECTION} + \underbrace{\mathcal{D}_C}_{MIXING} - \underbrace{\frac{\partial w_s C}{\partial z}}_{SETTLING} + \underbrace{\frac{E}{\delta z_b}\Big|_{z=z_b}}_{EROSION} \tag{18}$$

w_s is the settling velocity, dependent on sediment grain size, but not on flow conditions and concentrations (Soulsby, 1997). Settling is computed via a semi-Lagrangian advective flux algorithm, which is unconditionally stable (Durran, 2010). It uses a piece-wise parabolic vertical reconstruction of the suspended sediment for high-order interpolation, with WENO constraints to avoid oscillations. E is the erosion flux at the sea floor and is only applied to the first grid level of height z_b and cell size δz_b.

In the present study, this suspended sediment model is used with simple settings. It is composed of a single fine sand class with settling velocity w_s=2.5 cm s^{-1} (grain size d_{50}=0.22 mm). For resuspension, taking one sediment bed layer for simplicity, only two parameters are needed: the critical shear stress τ_{cr}, i.e., the threshold for initiation of sediment motion; and the erosion rate E_0 at the seafloor, expressed in the erosion flux formulation (Blaas et al., 2007):

$$E = E_0(1-p)\,\frac{\tau_b - \tau_{cr}}{\tau_{cr}} \quad \text{for } \tau_b > \tau_{cr} \tag{19}$$

E_0 and τ_{cr} are used for calibration but constrained by known empirical relationships: E_0 is set to 5.10^{-3} kg m^{-2} s^{-1} (Smith and McLean, 1977); τ_{cr} to 0.11 N m^{-2} (Soulsby and Whitehouse, 1997). p is the sediment porosity (0.41). τ_b is the bottom shear stress estimated from the logarithmic law of the wall:

$$\vec{\tau_b} = \frac{\kappa^2}{\log^2(\frac{z_b}{z_{0b}})}\,|u_b|\,\vec{u_b} \tag{20}$$

$|u_b|$ and $\vec{u_b}$ are the magnitude and vector of oceanic bottom currents in the log layer at a height z_b above bed; $\kappa = 0.41$ is the Von Karman constant; and z_{0b} is the bottom roughness length.

In the surfzone, the effect of wave-breaking, especially plunging breakers over sandbars, on sediment resuspension needs to be addressed (Voulgaris and Collins, 2000; van der Zanden et al., 2017; Otsuka et al., 2017; Lim et al., 2020). Lim et al. (2020) suggest a strong correlation between the maximum sediment concentration observed in the LIP experiment and the plunging point (about 10 m downstream of the breaking point) over the sandbar. We adopt here the approach proposed by Reniers et al. (2004) consisting in replacing $|u_b|$

by an stirring velocity reinforced by the turbulence motion induced by wave breaking:

$$u_{stir} = \sqrt{u_b^2 + u_t^2}$$
$$u_t = \phi(x)\,\alpha_{br}\,\sqrt{k_b} \tag{21}$$

The subgrid bottom turbulent kinetic energy k_b is given by the turbulence model and α_{br} is a factor explaining the effectiveness of breaking waves in the entrainment of bottom sediments. We used a common value of $\alpha_{br} = 10$ (Ribas et al., 2011), which produces sand concentrations close to observations in both the erosive and accretive phases. $\phi(x)$ is a Gaussian function centered around the plunging point in the bar trough (the standard deviation of about 10m corresponds to the size of the bar trough) in order to enhance the turbulence effect at this position. This increased efficiency in the trough of the bar may also reflect the effect of the large ripples observed in this region. In the absence of an appropriate parametrization for this effect, *phi* represents the only non-generic aspect of the present model application, but it is essential for reproducing the correct profiles of sediment concentrations — and in turn a condition for accurate bar migration. We have tried more generic parametrization of resuspension by plunging breakers with some success (see Discussion section) but a more dedicated study is needed for what appears to be a real challenge.

For bedload transport, we do not rely on parametrization as skewed-asymmetric waves are resolved explicitly, but we make sure that the wave-boundary layer is resolved, and that the first vertical level is in a sheet flow layer (about 10 times the grain size). This is particularly important for the onshore bar migration phase. However, some bedload processes are not resolved by the model, most notably the formation of small bedforms such as the observed centimeter-scale ripples in the bar trough. Estimating z_{0b} is not trivial with moving sediment and various empirical formulations exist that account for roughness over a mobile bed (Wiberg and Rubin, 1989). They generally assume that grain roughness is the most important predictor for the onset of sand suspension, but bedload and ripple form roughness are also considered (Li and Amos, 2001). We use grain roughness here, but assume that the effect of large ripples formed in the bar trough of LIP-1B and LIP-1C are included in the *phi* function and participates in the increased resuspension efficiency due to

turbulence.

2.6. Bed model and morphological acceleration

The bed model accounts for changes in sea floor elevation resulting from convergence or divergence in sediment fluxes (Exner equation):

$$\frac{\partial h}{\partial t} = -\frac{f_m}{\rho_s(1-p)}\left(w_s C - E\right) \tag{22}$$

ρ_s is sediment density and f_m is a morphological acceleration factor (Roelvink, 2006) described below. Morphological changes can have a significant influence on flow and transport when they are greater than a few percent of the water depth. Morphological updating strategies are described by Roelvink (2006) and implemented in CROCO following Warner et al. (2008). For dynamical consistency, the vertical velocity is modified by the rate of change of vertical grid levels dz/dt, adjusting to the moving sea floor and free surface (grid "breathing" component; Shchepetkin and McWilliams 2005). This method is mass conserving and retains tracer constancy preservation.

Morphological acceleration can be achieved with no constraint on the model time step by multiplying erosion and deposition rates by the scale factor f_m at the bed-water interface (Eq. 22). Only the fluxes to and from the bed are changed, not the magnitude of the sediment concentrations in the water column. To our knowledge, this paper presents the first use of a morphological acceleration technique with a wave-resolving model. We have found that the technique is effective since we obtain the same result with or without morphological acceleration. We were able to use a large morphological factor f_m (at least up to 72; Appendix B) because the timescale of morphodynamics (here bar migration) is slow compared to that of wave dynamics.

3. Simulation of a large-scale flume experiment

We now present our model solution of sandbar migration, applied to the European Large Installation Plan (LIP) experiments, which was carried out at full scale in Delft Hydraulics's

Delta Flume (Roelvink and Reniers, 1995). We first present the model setup for these experiments, the model validation of current profiles, then the comparative analysis of offshore and onshore bar migration.

3.1. LIP experiment

The Flume is 225 m long, 5 m wide and 7 m deep. In LIP, three types of experiments were carried out under different types of irregular waves, which subsequently resulted in a stable (1A), erosive (1B), and accretive (1C) beach state (see Table 1 and Roelvink and Reniers 1995 for details). The initial profile is linear in LIP-1A, with a slope of 1:30 and consisting of a median grain size of 0.22 mm. The final profile of LIP-1A was used as the initial profile of LIP-1B and the final profile of LIP-1B as the initial profile of LIP-1C. The wave conditions were a JONSWAP narrow-banded random wave spectrum generated by a wave paddle, with a peak enhancement factor $\gamma = 3.3$ and characteristic wave height and period: $H_s = 1.4$ m, $T_p = 5$ s (LIP-1B) and $H_s = 0.6$ m, $T_p = 8$ s (LIP-1C). Under this wave forcing, the sandbar developed during LIP-1B, increasing in height and migrating in the offshore direction. Under the accretive conditions of LIP-1C, the bar migration reversed to the onshore direction. The bed profile was measured with a profile follower that used an automated sounding system. Wave-averaged current profiles were captured by a movable carriage with attached current meters starting 10 cm above the bed and at 10 locations along the flume (2 cm/s accuracy). Similar profiles of wave-averaged concentrations of suspended sediment were measured by suction tubes mounted on a carriage starting 5 cm above the bed (10% accuracy). For validation of currents and sand concentration, we consider the time 8 hours after initialization in experiment 1B and 7 hours in 1C (Veen, 2014).

3.2. Model setup

The model setup is adapted from the LIP experiment. A JONSWAP wave spectrum similar to the experiment is generated with shore normal direction and zero directional spread. A no-slip condition is imposed on the lateral wall boundaries of the canal so that transverse modes are precluded. The grid spacing is dx=25 cm with 20 vertical levels with

refinement at the bottom (stretching parameter θ_b=8; see the documentation in www.croco-ocean.org). This vertical refinement is important for wave-related transport (Appendix B), while the results were poorly sensitive to horizontal resolution (a test with dx=50 cm and 1 m is presented below). The model time step is $dt = 25$ ms. The minimum depth is 1 mm on the shore, the position of which varies with the swash oscillation, relying on a wetting-drying scheme (Warner et al., 2013). For bed skin shear stress (setting sediment in motion), the logarithmic law of the wall is used with grain roughness $z_{0s} \sim D50/12 = 0.02$ mm. To account for increased momentum friction due to near-bed sediment suspension (e.g., Suarez et al. 2014), we increase the roughness length for momentum to 0.2 mm.

The LIP-1B and LIP-1C experiments lasted 18 and 13 hours, respectively. In both cases, the model was run for one hour with a morphological acceleration factor f_m equal to 18 and 13 respectively. Since the results were weakly sensitive to f_m (Appendix B), the acceleration technique allowed us to perform many sensitivity tests with even larger values.

3.3. Undertow's sensitivity to the turbulence model

An important process for offshore bar migration is the suspended load transport by the undertow. To assess the model hydrodynamics in the LIP configuration, we present a comparison of current profiles taken after 8 hours in experiment 1B and averaged over one hour. It will also be a test for our numerical wave maker in its ability to generate a spectrum of random waves.

Figure 1 shows a comparison of the model with data, using our standard configuration. The match with measured currents is very good throughout the complex morphology of the beach. The waves start to break before reaching the sandbar, but the breaking is more intense on the sandbar. The resulting velocity profile on the lee-side of the bar has a high shear and the undertow has an intensity above 30 cm/s. The horizontal resolution test (25 cm, 50 cm and 1 m) shows a root mean square error of about 3 cm/s at all resolutions, close to the measurement error of 2 cm/s. The results are thus consistent at all resolutions despite no adjustment of any parameter. It confirms the validity of a RANS approach for estimating the mixing length of breaking-induced turbulence.

Turbulent kinetic energy and eddy viscosity estimated by the k-ω model in the breaker zone have the expected structure (Fig. 1; top) and magnitude ($\nu_t \sim 0.01h\sqrt{gh}$; Svendsen 1987; Cox et al. 1994). Interestingly, the transport terms in the closure equations tend to reduce mixing at the break point by redistributing the turbulent energy, thus allowing more intense shear to be maintained (not shown). The k-ϵ model works almost as well as the k-ω model, with respect to mean current profiles, but the comparison is improved by imposing a high value on the surface mixing length (z_{0s}=0.2 m), as in wave-averaged models (Feddersen and Trowbridge, 2005). The k-ω model may thus be a better choice for surface wave breaking, possibly due to a more accurate near wall treatment (Mayer and Madsen, 2000; Brown et al., 2016; Devolder et al., 2018; Larsen et al., 2020). Note, however, that this model produces a greater amount of mixing in potential flow regions outside the surf zone (innershelf), mainly due to the divergence part of the mean strain rate tensor (Mayer and Madsen, 2000).

3.4. Currents and suspended sediments

To analyse the model for different conditions, two experiments are selected, namely LIP-1B and the LIP-1C cases (Table 1). Figure 2 shows a model-data comparison of wave height H_{rms} for the two experiments. The data is reproduced accurately. High waves in LIP-1B ($H_s = 1.4$ m, $T_p = 5$ s) caused beach erosion while, in LIP-1C, moderate waves ($H_s = 0.6$ m, $T_p = 8$ s) caused an accretive beach.

We are first interested in the erosion phase where the sandbar moves offshore under the effect of high waves. The LIP dataset is used for comparison purposes, containing velocity and concentration profiles as well as bed level evolution (see next section). Figure 3 shows a comparison of wave-mean velocity and concentration profiles for LIP-1B. As for velocity profiles presented in the validation section, sediment concentrations also show a very good match between model and data. The high concentrations over the sandbar crest and trough are triggered by a large bed shear stress associated with a combination of wave-mean undertow, wave oscillatory flow and turbulent velocity.

Note that waves and associated orbital velocities are greatest off the sandbar. However,

the maximum suspended sand concentration is not found offshore but coincides instead with a maximum in turbulence intensity and undertow speed inshore of the bar crest. This is in contrast to parametrizations more suited to shelf dynamics, where sediment erosion responds to the addition of bed shear stresses by currents and waves. (e.g., Soulsby 1995).

The model simulation of the accretive phase is also reproduced accurately (Figure 4). In this case, wave breaking occurs right on the sand bar. The currents are thus weaker off the bar, but the undertow inside the bar remains quite strong. The suspended sand concentration is also significant there, although weaker than in the erosive phase.

3.5. High-order velocity moments

In Marchesiello et al. (2021), the model's ability to simulate surface gravity wave propagation, nearshore breaking and the resulting circulation was validated against laboratory experiments. In particular, the GLOBEX scaled experiment (Michallet et al., 2014) provided high-resolution measurements of surface wave height η and bottom currents u_b. A comparison was made of continuous profiles of wave statistics for η and u_b across the beach. The model statistics closely resembled the measurement data (in structure and magnitude for both η and u_b), including high-order moments, showing the transition from skewness to asymmetry across the surfzone. More details can be found in Marchesiello et al. (2021).

The LIP experiment does not provide a high-resolution cross-shore profile but does provide access to vertical profiles at different positions around the sandbar. We can therefore make model-data comparisons of these vertical profiles for high-order velocity moments. Figure 5 shows the standard deviation $u_{rms} = \sqrt{\langle u'^2 \rangle}$, which is a measure of the intensity of the orbital wave velocity and the wave-mean flow variability in the surfzone. In experiments 1B and 1C, the model can faithfully reproduce the u_{rms} profiles. In experiment LIP-1B, u_{rms} is more intense than in experiment LIP-1C, particularly seaward of the sandbar, and in both cases there is a marked surface maximum of $\sim$1 m/s in the surfzone (which starts much further offshore in LIP-1B).

Then, we compare the third moment of the velocity, more precisely its normalized skewness: $S_u = \langle u'^3 \rangle / u_{rms}^3$. This is a measure of the nonlinear effects on the wave cycle, which

allows for residual transports. Figure 1 shows a model-data comparison of S_u for vertical profiles. Again, the ability of the model to reproduce the measured skewness is evident. In both the model and the data, there is an increase in skewness associated with shoaling and maximum values are near the surface ($\sim$2 or more). Note that the normalized skewness appears higher in the LIP-1C experiments. A more comprehensive analysis of the normalized and absolute skewness, its transition to asymmetry, and its impact on sediment transport is presented in Sections 4.2 and 4.3.

3.6. Offshore and onshore sandbar migration

Figure 7 (top) shows the bed evolution 18 hours after the start of experiment 1B, with the corresponding section of wave-mean cross-shore currents. Some small discrepancies are visible but the offshore sandbar migration is correctly reproduced in terms of distance of migration and height of the bar. The maximum undertow magnitude (-0.3 m/s) follows the lee-side slope of the bar and appears as the driver of its migration. A secondary undertow maximum is visible on the terrace of the inner surfzone and appears to coincide with an offshore spreading of the terrace. In the outer surfzone (off of the main sandbar), a second smaller bar forms both in the model and in the measurements during LIP-1B (at a position of about 70 m), corresponding to a weakened undertow.

The bottom panel of Figure 7 shows the result of the accretive phase LIP-1C when waves have lower amplitude, with an opposite migration directed towards the shore. In this case, the flow structure is very similar but weaker and the bar seems to migrate against the undertow. The latter is still able to bring sediment to the leeward slope of the bar, but the offshore slope and crest are moving inshore, creating an asymmetry in the bar shape.

4. Sediment transport mechanisms

4.1. Sediment budget

The wave-mean sediment transport term $-\frac{1}{\rho_0}\overline{\vec{\nabla}.(\rho\vec{\mathbf{v}}C)}$ — ρ_0 is a mean density, so that the transport term is in units of kg/m^3/s — is presented in Figure 8 for the time halfway between the erosive (top) or accretive (bottom) phase (averaged over a period of about 10 min). This

confirms for LIP-1B that during high waves and strong undertow, a large amount of sand is removed from the lee-side slope and trough area – after being first suspended and stirred upward – and then transported to the offshore slope, where it settles. Part of this process is attenuated by surface transport, which brings back some sediment to the bar trough region. For LIP-1C, however, sand is removed from both the trough of the bar and the offshore slope (including the crest), and it converges to the inner slope. This transport may qualify as bedload or sheet-flow transport as it occurs primarily within the wave boundary layer of about 10 cm.

For further analysis, Figure 9 presents the depth-integrated suspended sediment budget, again for the erosive (top) or accretive (bottom) phase. The different terms of Eq. 18 are computed online, averaged in time and integrated along the vertical axis. The budget comes down to three main tendency terms: erosion-settling residual, advection, and rate of change (vertical mixing cancels out when integrated). Suspended sediments are close to equilibrium since the rate of change is generally much smaller than the other two terms, which tend to be opposite. This analysis confirms the difference between LIP-1B and LIP-1C, with transport limited to the lee side of the bar in LIP-1C. In LIP-1B, there is a dominant erosion process in the bar trough and offshore transport and deposition beyond the bar crest. In LIP-1C, the process is similar but transport and deposition are confined to the inshore side of the bar crest, while a secondary zone of net erosion appears on the offshore side (this secondary erosion also appears in LIP-1B but much further offshore).

In the next section, we distinguish between wave and mean current transport in order to identify and quantify the role of asymmetric waves for bar migration, particularly in the accretion phase of LIP-1C.

4.2. Wave and current related fluxes

For each experiment (erosive or accretive), we construct an ensemble-averaged wave by superposing instantaneous data over 50 wave cycles. To that end, the duration of all wave cycles must be fitted to the peak period, so that data averaging can be made over the different phases of a generic cycle. This composite wave is made at three locations around

the sand bar: offshore slope, crest and trough (corresponding to positions: x=131, 139 and 148 m in LIP-1B; and x=129, 136 and 144 m in LIP-1C).

Starting with the more complex accretive case, Figure 10 (left panels) shows the currents and sand concentrations at the first model level (1-2 cm above bed) for the ensemble-averaged LIP-1C wave cycle. Here, the mean values are subtracted to retain the oscillatory flow and associated perturbed concentrations ($u' = u - \overline{u}$ and $C' = C - \overline{C}$). In addition, the figure shows the undertow u_b and effective turbulent velocity u_t entering the bed shear stress formulation. The currents have a typical skewed/asymmetric structure across the wave cycle. They are largely skewed over the offshore slope and become less skewed but more asymmetric as the wave progresses toward the shore. The largest sand concentrations are over the bar crest where it peaks about half a second after the peak velocity. The lag is similar for skewed velocity over the offshore slope, although the peak there is much weaker. The main reason is that the effective turbulent velocity is more than twice as large over the crest and more significantly contributes to the bed skin stress. The sand concentration cycle is different in the trough region, where the undertow becomes comparable in magnitude to the orbital velocities. The total onshore-directed flow is reduced during the crest half-cycle while the offshore-directed flow is increased during the trough half-cycle. As a result, positive resuspension anomalies are present during both phases of negative and positive wave velocities.

The right panels of Figure 10 show the profiles of suspended sand flux. The averaged flux over the composite wave cycle is separated into wave and mean components (Reynolds decomposition): $\overline{uC} = \overline{u'C'} + \overline{u}\,\overline{C}$. The undertow being weak over the offshore slope and crest (Fig. 7, bottom panel), the total flux there is dominated by the residual wave flux, which is onshore (at least in the wave boundary layer, but the flux is slightly negative above). The maximum flux over the crest appears to coincide with a combination of high sand concentration (1 g/L) and positive velocities (1 m/s) during the wave crest period (middle-right panel of Fig. 10). Over the offshore slope, the velocity is more skewed than asymmetric and the concentration is limited by a weaker bed stress (due to weaker turbulence). The phase lag between mobilization and transport of sediment (Dohmen-Janssen et al., 2002)

does not vary between the two positions (as expected from fast settling that gives a weak phase lag parameter) and therefore cannot explain the differences in sand flux. In the bar trough, the wave-related flux remains positive but its magnitude is much reduced. The reason is the second peak of sand resuspension during the wave trough phase (negative half-cycle), due to a strong undertow. An even stronger undertow could eventually reverse the sign of this flux (Scott et al., 2009).

The result of opposite onshore and offshore sand fluxes is a convergence of sediment between the trough and crest regions, which promotes an onshore bar migration. However, the bar takes on an asymmetric shape because the undertow plays a dominant role in the displacement of the bar crest.

In our simulations, wave-breaking turbulence contributes little to the onshore flux asymmetry, unlike in Ting and Kirby (1994). This is because, although more turbulent energy is generated at the surface during the wave crest period, a significant portion reaches the bottom during the trough of the next wave (Figure 1) and the bottom turbulent velocity in Figure 10 exhibits only small variations during the wave cycle. This tends to disprove a strong asymmetric effect of breaking turbulence, although we are aware that the turbulence model may misrepresent the role of plunging waves (i.e. the timing and efficiency with which they mobilize sediment). However, observations suggest that wave-breaking turbulence is sufficiently intermittent to lose some of its correlation with wave phase (Ruessink et al., 2011). Improvements could be made in this area.

Looking now at the LIP-1B erosive experiment (Fig. 11), we see a different dynamic, which generalizes the mechanism described earlier for the trough region. Since the undertow is present at all locations, the total flux is also negative at all locations. The wave-related flux tends to be weaker than in LIP-1C because the negative undertow decreases resuspension in the positive orbital velocity phase (wave crest) and increases it in the negative phase. However, over the crest, a significant wave-related flux remains. Note that waves over the sandbar in LIP-1B are actually weaker than in the accretive phase, despite larger offshore waves. The reason is that, in this case, the waves break offshore of the bar, where they lose much of their energy. However, the undertow extends across the sandbar and overwhelms

the wave effect everywhere. Note also the strong sediment flux convergence on the offshore side of the bar despite a consistently negative sand flux. In other words, there need not be a confluence of onshore and offshore fluxes for flux convergence to occur.

4.3. Wave asymmetry

Figure 12 presents the profiles of velocity skewness and asymmetry for the three sandbar locations. Normalized values (right panel) are computed as $\langle u'^3 \rangle / \langle u'^2 \rangle^{1.5}$ for skewness and $\langle \mathcal{H}(u')^3 \rangle / \langle u'^2 \rangle^{1.5}$ for asymmetry ($\mathcal{H}$ is Hilbert transform). Since a logarithmic scale is used, the asymmetry (which is negative) is presented with an inverse sign. We also present the dimensional values (right panel), calculated without normalization by the cube of standard deviations (on a normal scale with the correct signs). It confirms the relatively high skewness and low asymmetry on the outer slope, relative to the bar crest. The dimensional values reveal a much higher absolute asymmetry on the bar crest, compared to the surrounding areas. This result is hidden in the dimensionless calculation. Bottom skewness on the slope is larger than asymmetry on the crest, but with less effect on the sand flux, as seen earlier. This would confirm the efficiency of asymmetry versus skewness, but in our case this is coincidental: the difference in sand flux is related to the varying intensity of turbulence across the bar, rather than a varying phase lag between mobilization and transport — sometimes associated with the transformation from skewness to asymmetry (Dohmen-Janssen et al., 2002). Our interpretation of the respective role of asymmetry and skewness thus involves a spatial correlation between wave asymmetry and breaking turbulence. Finally, the trough region is characterized by low absolute skewness and asymmetry near the bed and the sand flux there is always driven by the undertow.

The dimensional skewness and asymmetry also reveal large vertical variations from surface to bottom. Wave skewness/asymmetry is intensified at the surface because wave velocities are greater, but the intensification is much larger for broken waves inshore of the bar. In this case, the wave velocities are also much stronger at the surface (1.2 m/s, as for shoaling waves) than at the bottom. Another noticeable point about these profiles is a slight decrease of dimensional skewness and asymmetry in the wave boundary layer, and

a decrease of dimensionless asymmetry in favor of skewness, consistent with observations (Suarez et al., 2014). However, here, this transformation is weak and does not seem to play a significant role.

4.4. Bed shear stress

It is interesting at this point to test the validity of formulations used for bed skin stress in wave-averaged models (e.g., Blaas et al. 2007). The friction is generally parametrized as the addition of wave-induced (τ_w) and current-induced (τ_{cw}) bottom stresses (Soulsby, 1995). In the nearshore region (as confirmed here), the current-related friction has a lesser role and we will focus on the friction induced by wave orbital velocities and breaking turbulence:

$$\tau_w = 0.5\, f_w\, (u_w + u_t)^2 \tag{23}$$

with the friction factor of (Soulsby, 1995), but modulated by a constant r_f:

$$f_w = 1.4\, r_f \left(\frac{u_w}{\sigma z_{0b}} \right)^{-0.52} \tag{24}$$

u_w is the maximum bottom orbital velocity, determined from wave-mean wave characteristics. u_w accounts for skewness as a correction to the linear theory (Isobe and Horikawa, 1982; Abreu et al., 2010; Malarkey and Davies, 2012; Nam et al., 2020): $u_w = r_s u_w^{lin}$, where r_s is a skewness factor ($r_s = 1$ for linear waves). r_s can be obtained using empirical formulas involving a logarithmic relation with the Ursell number $Ur = H_s \lambda^2 / h^3$, a measure of wave nonlinearity (Nam et al., 2020). Here, we use a slightly modified formula compared to Nam et al. (2020): $r_s = 0.051 \log Ur + 0.84$. The turbulence stirring velocity u_t is computed as for the wave-resolving simulation (Eq. 21) but with wave-averaged k_b.

Figure 13 shows our attempt of reconstructing the simulated bed shear stress with parametrizations. At offshore positions, where waves are nearly linear, a value of $r_f = 0.4$ is required to fit the simulated bed shear stress reconstructed from Soulsby (1995). Then, in the nearshore region from about $x = 40$ m, the parametrized bed shear stress is underestimated with linear waves and no turbulence ($r_s = 1$ and $u_t = 0$). Adding skewness correction, the bed shear stress is recovered more accurately around the sandbar, particularly on the

seaward side. The most striking feature is that turbulence stirring contributes most of the simulated stress on the sandbar (in the roller zone, downstream of the sandbar, the turbulence effect seems underestimated). This analysis thus confirms that consideration of wave asymmetry may be important but that turbulent mixing by plunging breakers is essential to mobilize significant sediment loads on the sandbar, allowing its realistic migration.

5. Discussion and conclusion

Analysing the interplay between wave-mean undertow and wave skewness/asymmetry in field measurements or even in physical models is a difficult task. Numerical modeling offers a complementary approach as long as their precision is not too compromised by unknown parameters. In the present study, we present the first application of a 3D wave-resolving hydro-sedimentary model to the case of bar migration. The simulation is that of a large-scale flume experiment comprising two phases: erosion (offshore bar migration) during high-wave conditions and accretion (onshore bar migration) during post-storm, moderate wave forcing. The model can faithfully reproduce in both cases the wave statistics, the profiles of wave-mean currents and sand concentrations, as well as the morphological evolution of the sand bed.

The analysis of the transport mechanisms shows the importance of the undertow distribution around the sandbar. Its convergence and divergence patterns appear to have more impact on submerged beach morphology than the confluence of wave- and current-related fluxes. In the erosion phase, in particular, the waves begin to break well ahead of the sandbar and a strong undertow causes the mobilized sediments to move in a near morphological translation. In this case, the wave-related transport is weak because sand mobilization, dominated by the undertow, is distributed almost uniformly between the two phases of the wave cycle. Much of the sediment is carried in suspension as the intensity of turbulence within the water column is high. It is interesting to note that there is a moderate surface flux of sediment towards the shore, carried by the breaker-induced onshore flow.

Under moderate wave action, the sandbar becomes a breaking point and the undertow is confined to the inshore area of the bar crest with a maximum on the inner slope. Because

the bed shear stress and associated mixing is weaker in this case, the sand concentration is almost confined to a sheet flow layer. In comparison to more energetic wave conditions, the sandbar migrates onshore at a slower rate and with an asymmetric shape. This is the result of a combination of two mechanisms: the deposition of sand carried by the undertow on the inshore side and, to a lesser extent, onshore fluxes due to asymmetric waves on the offshore side. Note that these mechanisms are not opposed here, as is often suggested (Roelvink and Stive, 1989; Grasso et al., 2011), but complementary.

The ensemble-averaged analysis of wave skewness/asymmetry reveals that the onshore sediment flux is strongest over the bar crest where asymmetry produces a steep front with strong currents during the onshore half-cycle. Associated with these currents, the sand is resuspended within only half a second with much contribution by breaking turbulence. Over the offshore slope, where skewness is greater than asymmetry, a similar process is at work but is weaker due to weaker resuspension, and not because of a greater phase lag between mobilization and transport.

These results thus confirm a moderate role of wave-related onshore flow in the evolution of sandbars, and only under post-storm wave conditions, when the sandbar becomes a breakpoint. The role of bottom streaming is unclear. By increasing bottom friction (roughness increased to 1 mm), it becomes a player, although not a dominant one in our simulations (it contributes a few cm/s and hardly counteracts the undertow of about 30 cm/s over the bar, even in the accretive case).

The largest uncertainty in the model comes from the estimation of bed roughness and bed shear stress due ripple formation and wave-breaking turbulence. Sand mobilization (and transport) does not appear realistic in the model without turbulence, as noted earlier by van der Zanden et al. (2017) and Lim et al. (2020) for the same LIP experiments. Lim et al. (2020) suggested that a large local increase of suspended sand concentration in the LIP experiment could only be attributed to breaker-induced turbulence and more precisely to plunging breaker vortices invading the wave bottom boundary layer. We followed the idea of Reniers et al. 2004 of adding a breaker-induced turbulent bottom current (from the turbulence model) to the bed shear stress formulation. Using an enhancement factor and

positioning function for this turbulent motion leads to realistic results. The positioning function, however, lacks a clear generic type mechanism and efforts should be made in this direction. This positioning coincide with the presence of large ripples in the bar trough and a parametrization of ripple formation may be a way to account for the increased resuspension efficiency in this area. Among the attempts we made, we found good results by setting the bottom roughness as a function of the undertow (the undertow seems to be a good proxy due to its correlation with breaker dissipation; Faria et al. 2000). Additional work will likely be required, including explicit consideration of plunging breakers.

Another feature of the present simulations is the absence of a bedload transport model. Our simulations suggest that the suspended load is the dominant mechanism driving the LIP sandbar migration, including sand fluxes associated with wave asymmetry in the wave boundary layer. In this sense, the bedload transport is at least partially solved but this would deserve further analysis. In particular, our simulations are limited to medium sands which have a rather low sedimentation velocity compared to the local bed friction velocity and are therefore easily suspended by waves. Application of the model to coarse sand beds may require a dedicated formula for bedload transport, including an avalanche process.

With these caveats in mind, our results nonetheless demonstrate the reliability of computationally efficient 3D wave-resolving models such as CROCO – intermediate between two-phase DNS and wave-averaged approaches – for addressing nearshore hydro-morphodynamic problems. They point out the deficiencies of the depth-averaged approach, with its hyper-sensitivity to bottom friction and rough estimation of the undertow, when its cross-shore distribution seems so important. Our wave-resolving model can also help improve parametrizations in 3D wave-averaged models, in particular wave-related transport through the concept of wave half-cycles (Shafiei et al., 2022).

An interesting new result also comes from the morphological acceleration method, which is used here for the first time with a wave-resolving model. We demonstrated its applicability and were even able to use a factor as large as 72, because the timescale of morphodynamics (here bar migration) is slow compared to that of wave dynamics. This method is particularly interesting in terms of computational cost because it allows us to consider long period

simulations despite the choice to explicitly solve for waves. Therefore, the possibility of using strong morphological acceleration in a wave-resolving approach makes it a suitable alternative to wave-averaged models for realistic 3D applications.

Acknowledgement

This research has received support from a consortium of French research agencies, as part of CROCO's development project (Insu GdR n°2014 named CROCO) and from the French Naval Hydrographic and Oceanographic Service (SHOM DGA-Protevs II and MEPELS projects). It was granted access to the HPC resources of CALMIP supercomputing center under allocation P19069. We thank Dano Roelvink for sharing the LIP data. Apart from these, all data were acquired by the authors and the CROCO source code is freely available at `www.croco-ocean.org`. Both laboratory and modeling data are available upon request.

Appendix A. Time-splitting procedure

The compressible Navier-Stokes equations require a relation between ρ and P. To that end, and as part of a time-splitting approach, density is decomposed into slow and fast components based on a first-order linear decomposition with respect to total pressure (Auclair et al., 2018; Marchesiello et al., 2021). In the following, s and f subscripts refer to slow and fast-mode components respectively:

$$\rho = \rho_s(T,S,P_s) + \overbrace{\left.\frac{\partial \rho}{\partial P}\right|_{T,S}}^{\rho_f = c_s^{-2} P_f} \delta P + O(\delta P^2) \tag{A.1}$$

$$P = \underbrace{P_{atm} + \int_z^\eta (\rho_s - \rho_0) g \, dz'}_{SLOW} + \underbrace{\rho_0 g(\eta - z) + \overbrace{\delta P}^{P_f}}_{FAST} \tag{A.2}$$

c_s is the speed of sound and $\delta P = P_f$ is the nonhydrostatic pressure.

The Navier-Stokes equations are then integrated with two different time steps within the time-splitting approach inherited from ROMS. The slow-mode integration is similar to

ROMS, with the addition of the slow part of vertical momentum equation, while the fast-mode integration is in 3D and includes the compressible terms of momentum and continuity equations. In vector form:

$$\frac{\partial \rho \vec{\mathbf{v}}}{\partial t} = \underbrace{-\vec{\nabla}.(\rho \vec{\mathbf{v}} \otimes \vec{\mathbf{v}}) - 2\rho\vec{\Omega} \times \vec{\mathbf{v}} - \vec{\nabla}(\int_z^{\eta_f} (\rho_s - \rho_0) g \; dz') + \vec{\mathcal{F}}_{\vec{\mathbf{v}}} + \vec{\mathcal{D}}_{\vec{\mathbf{v}}}}_{SLOW}$$
$$\underbrace{-\rho_0 g \vec{\nabla}\eta_f - \vec{\nabla} P_f + \rho_f \vec{\mathbf{g}} + \lambda \vec{\nabla}(\vec{\nabla}.\vec{\mathbf{v}})}_{FAST} \tag{A.3}$$

$$\frac{\partial \rho_f}{\partial t} = -\frac{\partial \rho_s}{\partial t} - \vec{\nabla}.(\rho \vec{\mathbf{v}}) \tag{A.4}$$

$$P_f = c_s^2 \; \rho_f \tag{A.5}$$

$$\frac{\partial \eta_f}{\partial t} = \; w_f|_{z=\eta} - \vec{\mathbf{v}}_f|_{z=\eta}.\vec{\nabla}\eta_f \tag{A.6}$$

$$\frac{\partial \rho C_s}{\partial t} = -\vec{\nabla}.(\rho \vec{\mathbf{v}} C_s) + \mathcal{F}_C + \mathcal{D}_C \tag{A.7}$$

$$\rho_s = \rho(T_s, S_s, \eta_f) \tag{A.8}$$

$$\rho = \rho_s + \rho_f \tag{A.9}$$

The momentum is integrated both in slow and fast modes but the right-hand-side of the equation is split in two parts: a slow part, made of slowly varying terms (advection, Coriolis force, baroclinic pressure force and viscous dissipation), and a fast part, made of fast-varying terms (the surface-induced and compressible pressure force, weight, and dissipation associated with bulk-viscosity). This momentum equation is numerically integrated twice, once with a large time-step keeping the fast part constant, and once with a smaller time-step keeping the slow part constant. This is much more computationally efficient than integrating the whole set of equations at the same fast time step.

Appendix B. Model sensitivity to morphological acceleration and vertical resolution

We briefly present some of the sensitivities of the morphological evolution to the model parameters during the erosion phase 1B (Fig. 14). First, the reliability of the morphological factor is assessed by testing a value of f_m four times larger than in the standard run: 72 instead of 18. In this case, the model is run for 20 minutes (about 10 min wall-clock time on a 4 processor machine) instead of the actual 18-hour experiment that would be required if no acceleration was performed (f_m=1). After 18 hours, the difference in morphological evolution between the simulations with f_m of 18 and 72 is very small, even in the sandbar area, which is the most active. We did not increase f_m further because it would start affecting the statistics of wave spectrum.

A more sensitive parameter is the vertical resolution. We tested a simulation with 10 vertical levels instead of 20 (Fig. 14). In this case, the current-related offshore transport is less affected than the wave-related onshore transport. This is because the latter occurs in a wave boundary layer of about 10 cm width that requires at least a few grid points to be resolved (see Sect. 4.2). Therefore, with weaker onshore transport, the bar migrates a few meters farther offshore than in the laboratory experiment and in the 20-level simulation.

References

Abreu, T., Silva, P.A., Sancho, F., Temperville, A., 2010. Analytical approximate wave form for asymmetric waves. Coastal Engineering 57, 656–667.

Alberello, A., Chabchoub, A., Gramstad, O., Babanin, A.V., Toffoli, A., 2016. Non-gaussian properties of second-order wave orbital velocity. Coastal Engineering 110, 42–49.

Almar, R., Castelle, B., Ruessink, B.G., Sénéchal, N., Bonneton, P., Marieu, V., 2010. Two- and three-dimensional double-sandbar system behaviour under intense wave forcing and a meso–macro tidal range. Continental Shelf Research 30, 781–792.

Auclair, F., Bordois, L., Dossmann, Y., Duhaut, T., Paci, A., Ulses, C., Nguyen, C., 2018. A non-hydrostatic non-boussinesq algorithm for free-surface ocean modelling. Ocean Modelling 132.

Blaas, M., Dong, C., Marchesiello, P., McWilliams, J.C., Stolzenbach, K.D., 2007. Sediment-transport modeling on southern californian shelves: A ROMS case study. Continental Shelf Research 27, 832 – 853.

685 Blayo, E., Debreu, L., 2005. Revisiting open boundary conditions from the point of view of characteristic
686 variables. Ocean Modelling 9, 231–252.
687 Borges, R., Carmona, M., Costa, B., Don, W.S., 2008. An improved weighted essentially non-oscillatory
688 scheme for hyperbolic conservation laws. Journal of Computational Physics 227, 3191 – 3211.
689 Brown, S., Greaves, D.M., Magar, V., Conley, D.C., 2016. Evaluation of turbulence closure models under
690 spilling and plunging breakers in the surf zone. Coastal Engineering 114, 177–193.
691 Burchard, H., Petersen, O., Rippeth, T.P., 1998. Comparing the performance of the mellor-yamada and the
692 $k - \epsilon$ two-equation turbulence models. Journal of Geophysical Research: Oceans 103, 10543–10554.
693 Chauchat, J., Cheng, Z., Nagel, T., Bonamy, C., Hsu, T.J., 2017. Sedfoam-2.0: a 3-d two-phase flow
694 numerical model for sediment transport. Geoscientific Model Development 10, 4367–4392.
695 Chen, Q., Wu, W., Zhu, L., 2018. Recent Developments in Numerical Modeling of Coastal Hydrodynamics
696 and Sediment Transport. chapter Chapter 5. pp. 145–197.
697 Cheng, Z., Hsu, T.J., Calantoni, J., 2017. Sedfoam: A multi-dimensional eulerian two-phase model for
698 sediment transport and its application to momentary bed failure. Coastal Engineering 119, 32–50.
699 Cox, D.T., Kobayashi, N., Okayasu, A., 1994. Vertical Variations of Fluid Velocities and Shear Stress in
700 Surf Zones. pp. 98–112.
701 Debreu, L., Marchesiello, P., Penven, P., Cambon, G., 2012. Two-way nesting in split-explicit ocean models:
702 Algorithms, implementation and validation. Ocean Modelling 49–50, 1 – 21.
703 Derakhti, M., Kirby, J.T., 2014. Bubble entrainment and liquid–bubble interaction under unsteady breaking
704 waves. Journal of Fluid Mechanics 761, 464–506.
705 Derakhti, M., Kirby, J.T., Shi, F., Ma, G., 2016. Nhwave: Consistent boundary conditions and turbulence
706 modeling. Ocean Modelling 106, 121 – 130.
707 Devolder, B., Troch, P., Rauwoens, P., 2018. Performance of a buoyancy-modified $k - \omega$ and $k - \omega$ sst
708 turbulence model for simulating wave breaking under regular waves using openfoam. Coastal Engineering
709 138, 49–65.
710 Dibajnia, M., Watanabe, A., 1992. Sheet flow under nonlinear waves and currents. Coastal Engineering
711 Proceedings 1.
712 Dohmen-Janssen, C., Kroekenstoel, D.F., Hassan, W.N., Ribberink, J.S., 2002. Phase lags in oscillatory
713 sheet flow: experiments and bed load modelling. Coastal Engineering 46, 61–87.
714 Drake, T.G., Calantoni, J., 2001. Discrete particle model for sheet flow sediment transport in the nearshore.
715 Journal of Geophysical Research: Oceans 106, 19859–19868.
716 Durran, D.R., 2010. Numerical Methods for Fluid Dynamics: With Applications to Geophysics. volume 32
717 of Texts in Applied Mathematics. Springer.
718 Elgar, S., Gallagher, E.L., Guza, R.T., 2001. Nearshore sandbar migration. Journal of Geophysical Research:

719 Oceans 106, 11623–11627.
720 Faria, A., Thornton, E., Lippmann, T., Stanton, T., 2000. Undertow over a barred beach. Journal of
721 Geophysical Research 105, 16999–17010.
722 Feddersen, F., Trowbridge, J., 2005. The effect of wave breaking on surf-zone turbulence and alongshore
723 currents: A modeling study. Journal of Physical Oceanography 35.
724 Grasso, F., Michallet, H., Barthélemy, E., 2011. Sediment transport associated with morphological beach
725 changes forced by irregular asymmetric, skewed waves. Journal of Geophysical Research: Oceans 116.
726 Hsu, T.J., Hanes, D.M., 2004. Effects of wave shape on sheet flow sediment transport. Journal of Geophysical
727 Research: Oceans 109.
728 Isobe, M., Horikawa, K., 1982. Study on water particle velocities of shoaling and breaking waves. Coastal
729 Engineering in Japan 25, 109–123.
730 Kalra, T., Sherwood, C., Warner, J., Rafati, Y., Hsu, T.J., 2019. Investigating bedload transport under
731 asymmetrical waves using a coupled ocean-wave model. pp. 591–604.
732 Kim, Y., Mieras, R.S., Cheng, Z., Anderson, D., Hsu, T.J., Puleo, J.A., Cox, D., 2019. A numerical
733 study of sheet flow driven by velocity and acceleration skewed near-breaking waves on a sandbar using
734 sedwavefoam. Coastal Engineering 152, 103526.
735 Klemp, J.B., Skamarock, W.C., Ha, S., 2018. Damping acoustic modes in compressible horizontally explicit
736 vertically implicit (hevi) and split-explicit time integration schemes. Monthly Weather Review 146, 1911
737 – 1923.
738 Larsen, B.E., van der A, D.A., van der Zanden, J., Ruessink, G., Fuhrman, D.R., 2020. Stabilized rans
739 simulation of surf zone kinematics and boundary layer processes beneath large-scale plunging waves over
740 a breaker bar. Ocean Modelling 155, 101705.
741 Li, M.Z., Amos, C.L., 2001. Sedtrans96: the upgraded and better calibrated sediment-transport model for
742 continental shelves. Computers and Geosciences 27, 619–645. Numerical Models of Marine Sediment
743 Transport and Deposition.
744 Lim, G., Jayaratne, R., Shibayama, T., 2020. Suspended sand concentration models under breaking waves:
745 Evaluation of new and existing formulations. Marine Geology 426, 106197.
746 Lin, P., Liu, P.L.F., 1998. A numerical study of breaking waves in the surf zone. Journal of Fluid Mechanics
747 359, 239–264.
748 Long, W., Kirby, J.T., Hsu, T.J., . Cross shore sandbar migration predicted by a time domain boussinesq
749 model incorporating undertow. pp. 2655–2667.
750 Malarkey, J., Davies, A., 2012. Free-stream velocity descriptions under waves with skewness and asymmetry.
751 Coastal Engineering 68, 78–95.
752 Marchesiello, P., Auclair, F., Debreu, L., McWilliams, J., Almar, R., Benshila, R., Dumas, F., 2021. Tridi-

753 mensional nonhydrostatic transient rip currents in a wave-resolving model. Ocean Modelling 163, 101816.
754 Marchesiello, P., McWilliams, J.C., Shchepetkin, A., 2001. Open boundary conditions for long-term inte-
755 gration of regional oceanic models. Ocean modelling 3, 1–20.
756 Mayer, S., Madsen, P.A., 2000. Simulation of Breaking Waves in the Surf Zone using a Navier-Stokes Solver.
757 pp. 928–941.
758 McWilliams, J.C., Restrepo, J.M., Lane, E.M., 2004. An asymptotic theory for the interaction of waves and
759 currents in coastal waters. Journal of Fluid Mechanics 511, 135–178.
760 Michallet, H., Ruessink, B.G., Vieira Lima Matias da Rocha, M., De Bakker, A., Van Der A, D.A., Ruju,
761 A., Silva, P.A., Sénéchal, N., Marieu, V., Tissier, M., Almar, R., Abreu, T., Birrien, F., Vignal, L.,
762 Barthélemy, E., Mouazé, D., Cienfuegos, R., Wellens, P., 2014. GLOBEX: Wave dynamics on a shallow
763 sloping beach, in: HYDRALAB IV Joint User Meeting, Lisbon, July 2014, Lisbonne, Portugal. pp. 1–12.
764 Nam, P.T., Staneva, J., Thao, N.T., Larson, M., 2020. Improved calculation of nonlinear near-bed wave
765 orbital velocity in shallow water: Validation against laboratory and field data. Journal of Marine Science
766 and Engineering 8.
767 Otsuka, J., Saruwatari, A., Watanabe, Y., 2017. Vortex-induced suspension of sediment in the surf zone.
768 Advances in Water Resources 110, 59–76.
769 Rafati, Y., Hsu, T.J., Elgar, S., Raubenheimer, B., Quataert, E., van Dongeren, A., 2021. Modeling the
770 hydrodynamics and morphodynamics of sandbar migration events. Coastal Engineering 166, 103885.
771 Reniers, A.J.H.M., Roelvink, J.A., Thornton, E.B., 2004. Morphodynamic modeling of an embayed beach
772 under wave group forcing. Journal of Geophysical Research: Oceans 109.
773 Ribas, F., de Swart, H., Calvete, D., Falqués, A., 2011. Modeling waves, currents and sandbars on natural
774 beaches: The effect of surface rollers. Journal of Marine Systems 88, 90–101. 41st International Liege
775 Colloquium on Ocean Dynamics"Science based management of the coastal waters.
776 Roelvink, D., Roelvink, J., Reniers, A., 2012. A Guide to Modeling Coastal Morphology. Advances in
777 coastal and ocean engineering, World Scientific.
778 Roelvink, J., 2006. Coastal morphodynamic evolution techniques. Coastal Engineering 53, 277–287. Coastal
779 Hydrodynamics and Morphodynamics.
780 Roelvink, J.A., Reniers, 1995. IP 11D delta flume experiments : a dataset for profile model validation. WL
781 / Delft Hydraulics.
782 Roelvink, J.A., Stive, M.J.F., 1989. Bar-generating cross-shore flow mechanisms on a beach. Journal of
783 Geophysical Research: Oceans 94, 4785–4800.
784 Ruessink, B.G., Michallet, H., Abreu, T., Sancho, F., Van der A, D.A., Van der Werf, J.J., Silva, P.A., 2011.
785 Observations of velocities, sand concentrations, and fluxes under velocity-asymmetric oscillatory flows.
786 Journal of Geophysical Research: Oceans 116.

Schnitzler, B., 2015. Modeling sand transport under breaking waves.

Scott, N.V., Hsu, T.J., Cox, D., 2009. Steep wave, turbulence, and sediment concentration statistics beneath a breaking wave field and their implications for sediment transport. Continental Shelf Research 29, 2303–2317.

Shafiei, H., Chauchat, J., Bonamy, C., Marchesiello, P., 2022. Adaptation of the santoss transport formula for 3d nearshore models: application to cross-shore sandbar migration. Ocean Modelling in revision.

Shchepetkin, A.F., McWilliams, J.C., 2005. The regional oceanic modeling system (roms): a split-explicit, free-surface, topography-following-coordinate oceanic model. Ocean Modelling 9, 347–404.

Smith, J.D., McLean, S.R., 1977. Spatially averaged flow over a wavy surface. Journal of Geophysical Research (1896-1977) 82, 1735–1746.

Soufflet, Y., Marchesiello, P., Lemarié, F., Jouanno, J., Capet, X., Debreu, L., Benshila, R., 2016. On effective resolution in ocean models. Ocean Modelling 98, 36–50.

Soulsby, R., 1995. Bed shear stresses due to combined waves and currents, in: Stive, M., Fredsøe, J., Hamm, L., Soulsby, R., Teisson, C., Winterwerp, J. (Eds.), Advances in Coastal Morphodynamics, Delft Hydraulics, Delft, The Netherlands. pp. 420–423.

Soulsby, R., 1997. Dynamics of marine sands. Thomas Telford Publishing.

Soulsby, R., Whitehouse, R., 1997. Threshold of sediment motion in coastal environments.

Stive, M., 1986. A model for cross-shore sediment transport, in: Procedings of the 20th International Conference on Coastal Engineering, American Society of Civil Engineers, New York.

Suarez, L., Barthelemy, E., Berni, C., Chauchat, J., Michallet, H., Cienfuegos, R., 2014. Vertical distribution of skewness and asymmetry in a boundary layer on a mobile bed. experiment and k-ω comparison. La Houille Blanche , 88–94.

Svendsen, I., 1987. Analysis of surf zone turbulence. Journal of Geophysical Research: Oceans 92, 5115–5124.

Thornton, E.B., Humiston, R.T., Birkemeier, W., 1996. Bar/trough generation on a natural beach. Journal of Geophysical Research: Oceans 101, 12097–12110.

Ting, F.C., Kirby, J.T., 1994. Observation of undertow and turbulence in a laboratory surf zone. Coastal Engineering 24, 51–80.

van der A, D.A., Ribberink, J.S., van der Werf, J.J., O'Donoghue, T., Buijsrogge, R.H., Kranenburg, W.M., 2013. Practical sand transport formula for non-breaking waves and currents. Coastal Engineering 76, 26–42.

van der Zanden, J., van der A, D., Hurther, D., Cáceres, I., O'Donoghue, T., Ribberink, J., 2017. Suspended sediment transport around a large-scale laboratory breaker bar. Coastal Engineering 125, 51–69.

van Rijn, L., Walstra, D., Grasmeijer, B., Sutherland, J., Pan, S., Sierra, J., 2003. The predictability of cross-shore bed evolution of sandy beaches at the time scale of storms and seasons using process-based

821 profile models. Coastal Engineering 47, 295–327.
822 Veen, R., 2014. The implementation and testing of the santoss sand transport model in delft3d.
823 Voulgaris, G., Collins, M., 2000. Sediment resuspension on beaches: response to breaking waves. Marine
824 Geology 167, 167–187.
825 Warner, J., Sherwood, C., Arango, H., Signell, R., 2005. Performance of four turbulence closure methods
826 implemented using a generic length scale method. Ocean Modelling 8, 81–113.
827 Warner, J.C., Defne, Z., Haas, K., Arango, H.G., 2013. A wetting and drying scheme for ROMS. Computers
828 and Geosciences 58, 54 – 61.
829 Warner, J.C., Sherwood, C.R., Signell, R.P., Harris, C.K., Arango, H.G., 2008. Development of a three-
830 dimensional, regional, coupled wave, current, and sediment-transport model. Computers & Geosciences
831 34, 1284–1306.
832 Watanabe, A., 1982. Numerical models of nearshore currents and beach deformation. Coastal Engineering
833 in Japan 25, 147–161.
834 Watanabe, Y., Saeki, H., 1999. Three-dimensional large eddy simulation of breaking waves. Coastal Engi-
835 neering Journal 41, 281–301.
836 van der Werf, J., Veen, R., Ribberink, J., van der Zanden, J., 2015. Testing of the new santoss transport
837 formula in the Delft3d morphological modeling system.
838 Wiberg, P.L., Rubin, D.M., 1989. Bed roughness produced by saltating sediment. Journal of Geophysical
839 Research: Oceans 94, 5011–5016.
840 Wilcox, D.C., 1988. Reassessment of the scale-determining equation for advanced turbulence models. AIAA
841 Journal 26, 1299–1310.
842 Zijlema, M., Stelling, G., Smit, P., 2011. Swash: An operational public domain code for simulating wave
843 fields and rapidly varied flows in coastal waters. Coastal Engineering 58, 992 – 1012.

Table 1: LIP experiment conditions from Roelvink and Reniers (1995)

Experiment	Initial Geometry	H_S [m]	T_P [s]	Duration [h]	Collection [h]
LIP11-1A	Initial beach profile	0.9	5	12	
LIP11-1B	Result of 1A	1.4	5	18	8
LIP11-1C	Result of 1B	0.6	8	13	7

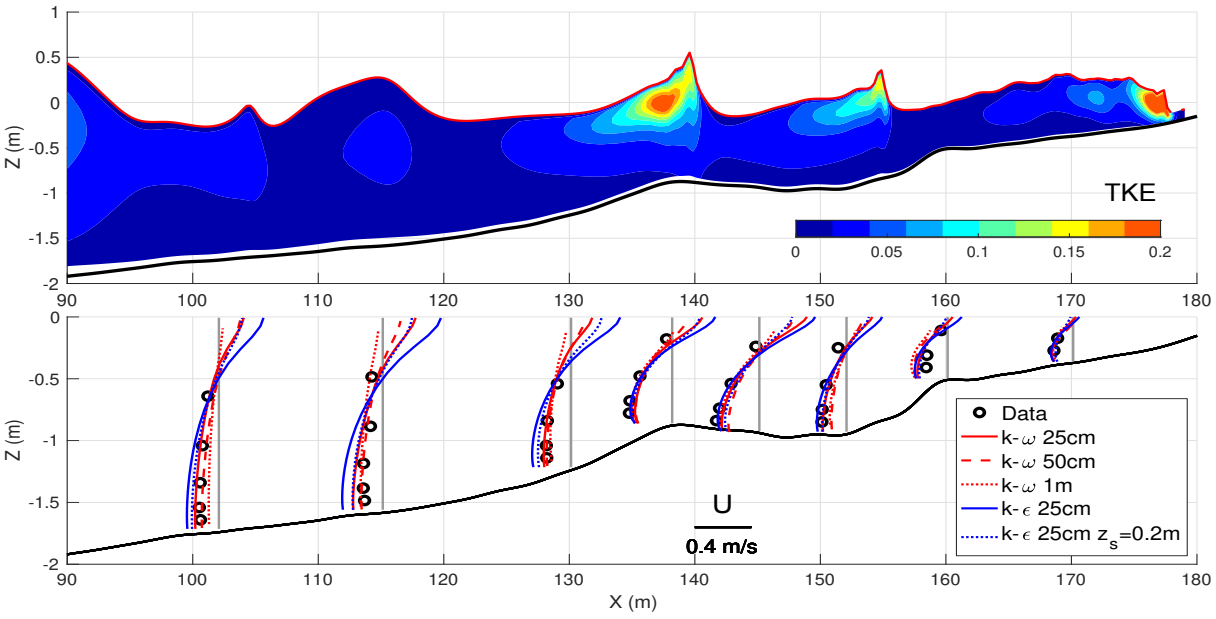

Figure 1: Model comparison with the large-scale LIP11-1B Flume experiment. Top) Snapshot of wave height and turbulent kinetic energy k $[m^2/s^2]$ from the reference model simulation (25 cm resolution; k-ω turbulence model). Bottom) Comparison of simulated and measured cross-shore current profiles: sensitivity to resolution (25 cm, 50 cm and 1 m) and turbulence models (k-ω in red; k-ϵ in blue).

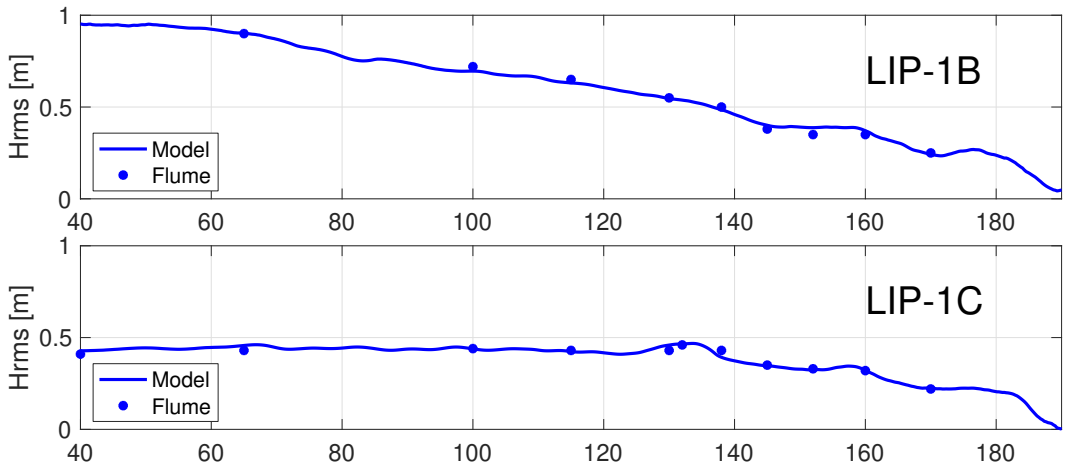

Figure 2: Model-data comparison of H_{rms} in LIP Flume experiment (top: 1B; bottom: 1C).

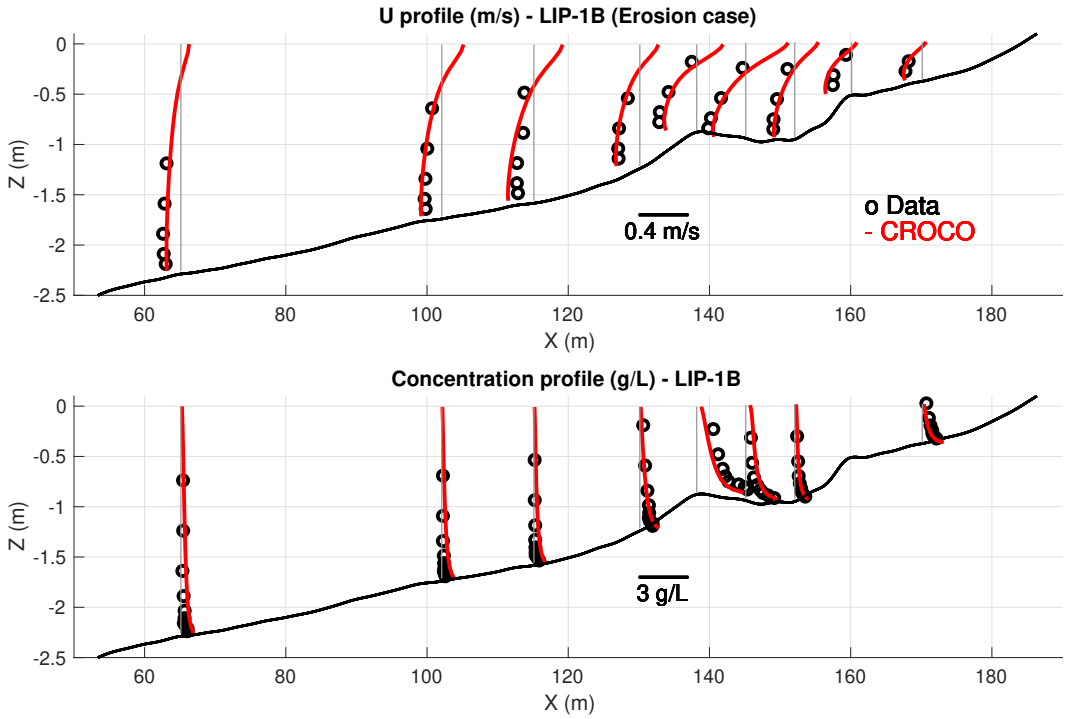

Figure 3: Model-data comparison of wave-mean cross-shore velocity and sand concentration profiles in the erosive LIP11-1B Flume experiment.

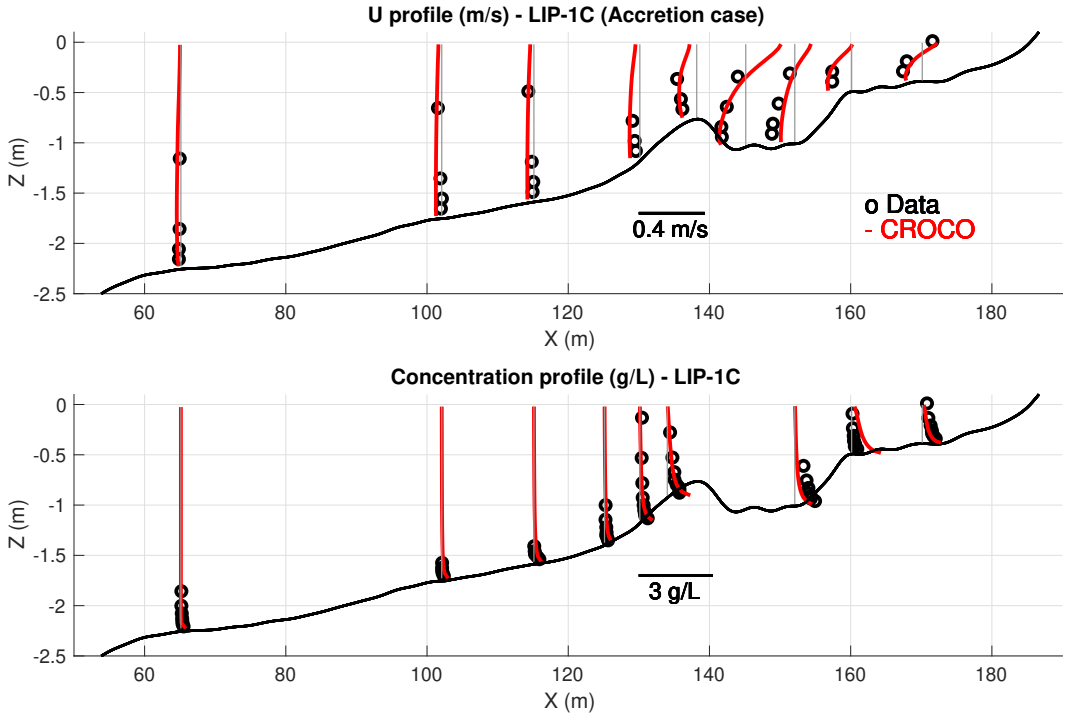

Figure 4: Model-data comparison of wave-mean cross-shore velocity and sand concentration profiles in the accretive LIP11-1C Flume experiment.

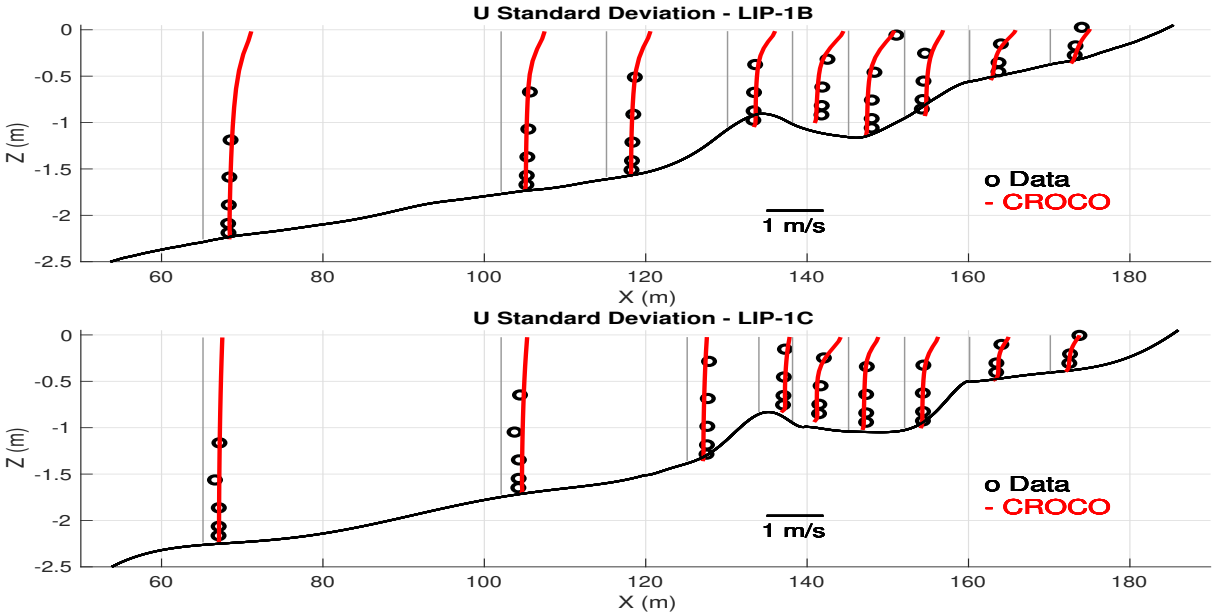

Figure 5: Model-data comparison of velocity standard deviation profiles in the LIP11-1B and LIP11-1C experiments.

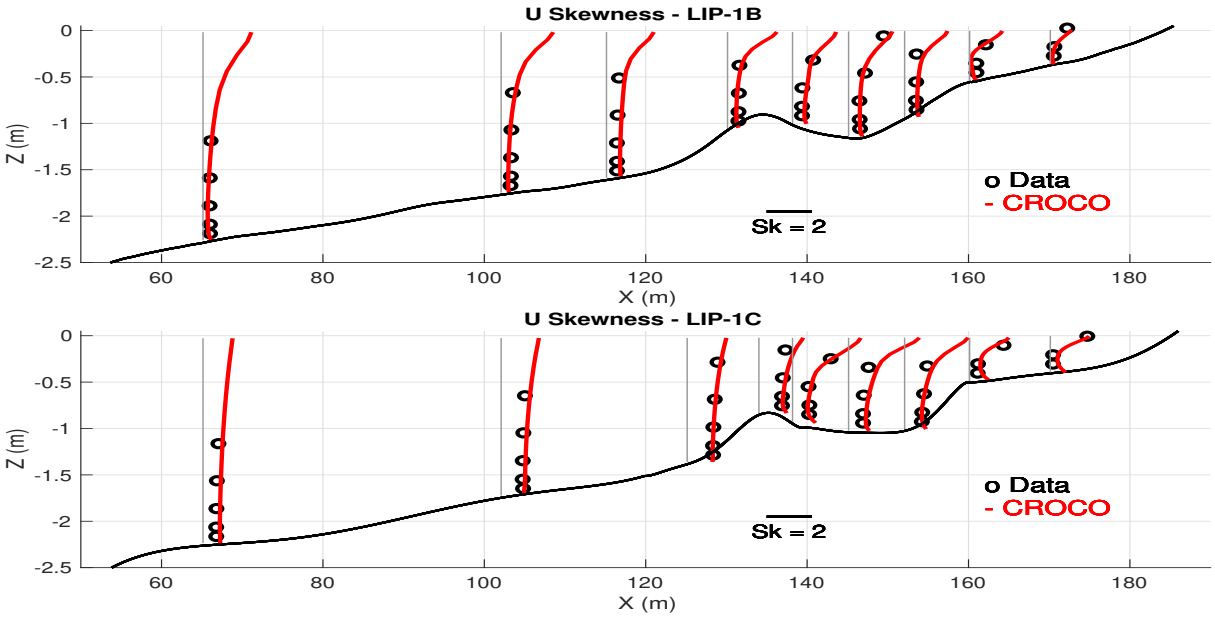

Figure 6: Model-data comparison of velocity skewness profiles in the LIP11-1B and LIP11-1C experiments.

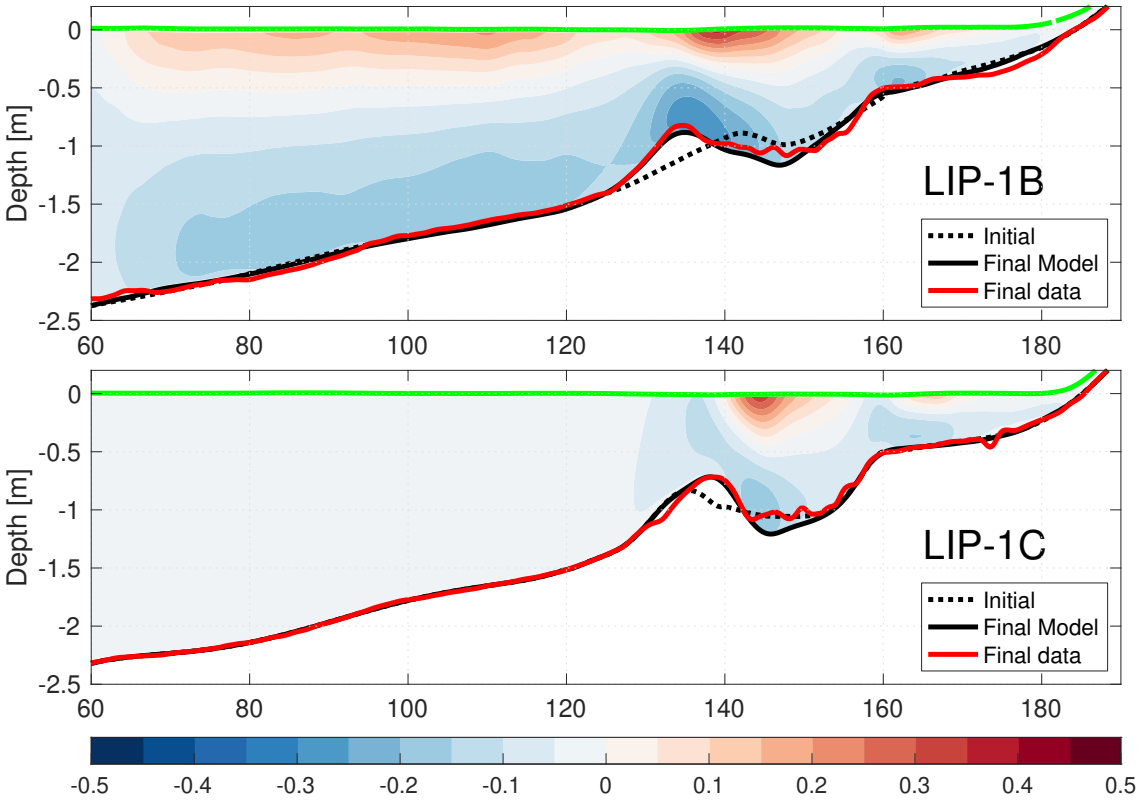

Figure 7: Model comparison of morphological changes with LIP measurements during the erosion phase (LIP-1B) and accretion phase (LIP-1C). Wave-mean cross-shore velocities are also shown in filled contours [m/s].

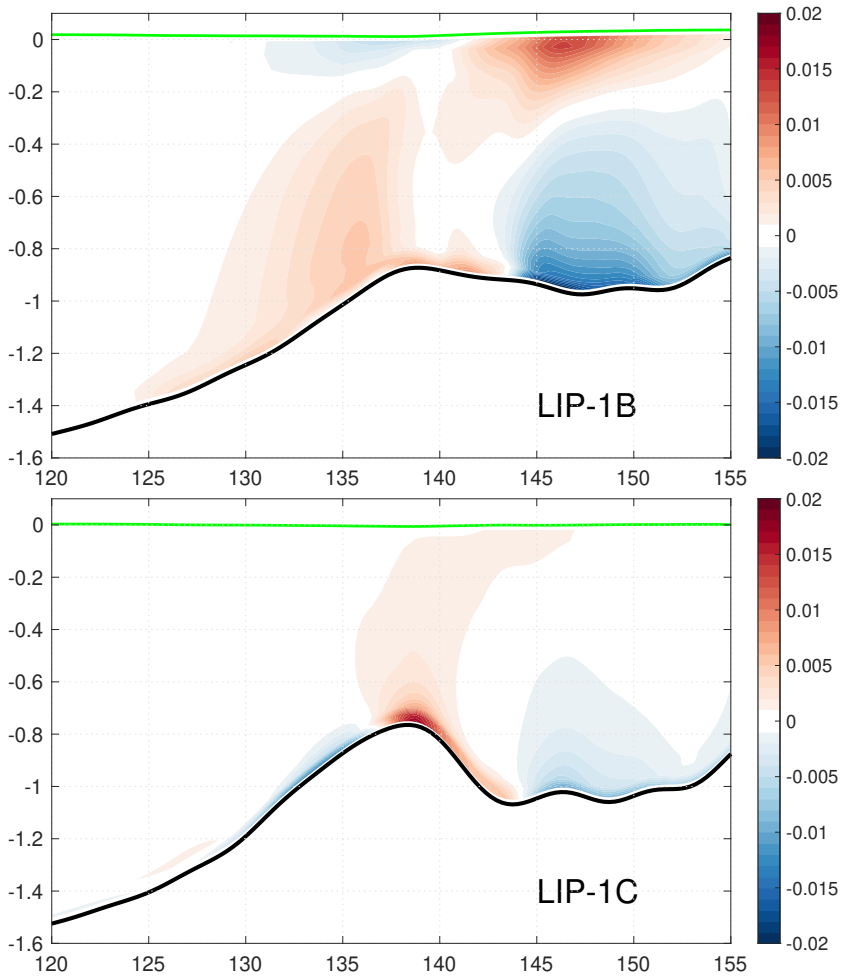

Figure 8: Wave-mean sand advection [kg/m^3/s] halfway through the erosion phase (LIP-1B) and accretion phase (LIP-1C). Positive (negative) values indicate a gain (loss) in sand concentration due to transport.

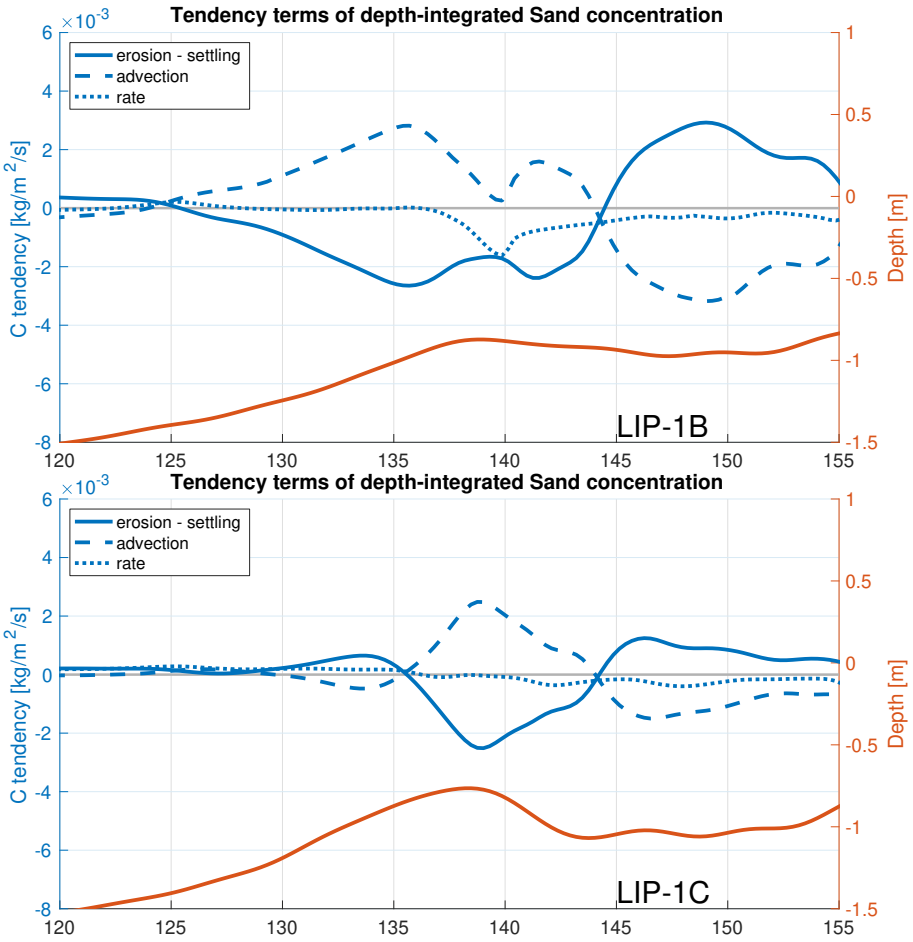

Figure 9: Depth-integrated budget of sand concentration halfway through the erosion phase (LIP-1B) and accretion phase (LIP-1C).

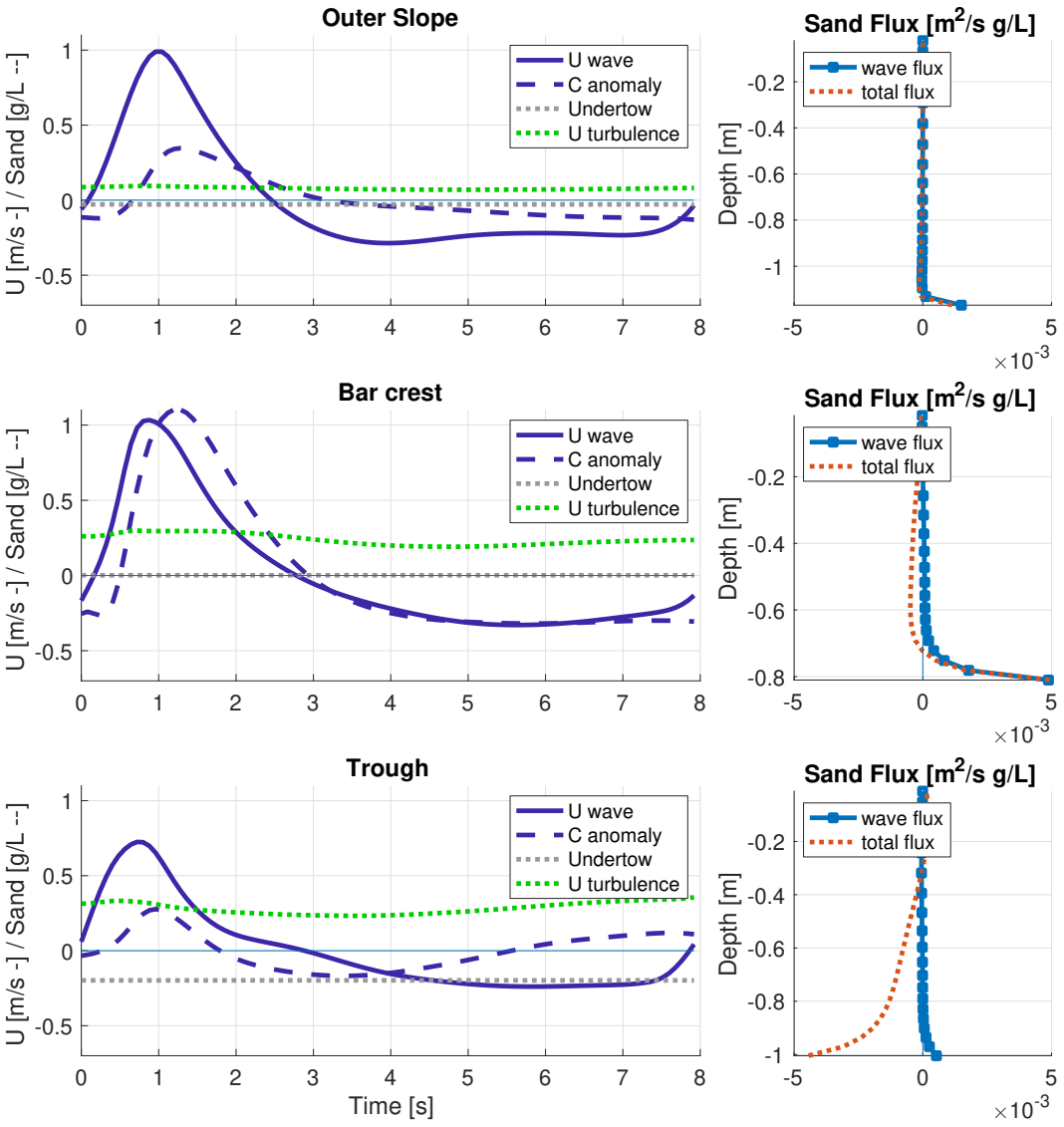

Figure 10: Left panels: ensemble-averaged wave cycle of current and sand concentration anomaly ($u' = u - \overline{u}$ and $C' = C - \overline{C}$) at three positions over the sandbar during the accretive LIP-1C Flume experiment. The wave-mean undertow u_b and mean effective turbulent velocity u_t at the bottom level z_b are also represented. Right panels: profiles of suspended sand flux (total flux: $\overline{uC}$; and wave flux: $\overline{u'C'}$).

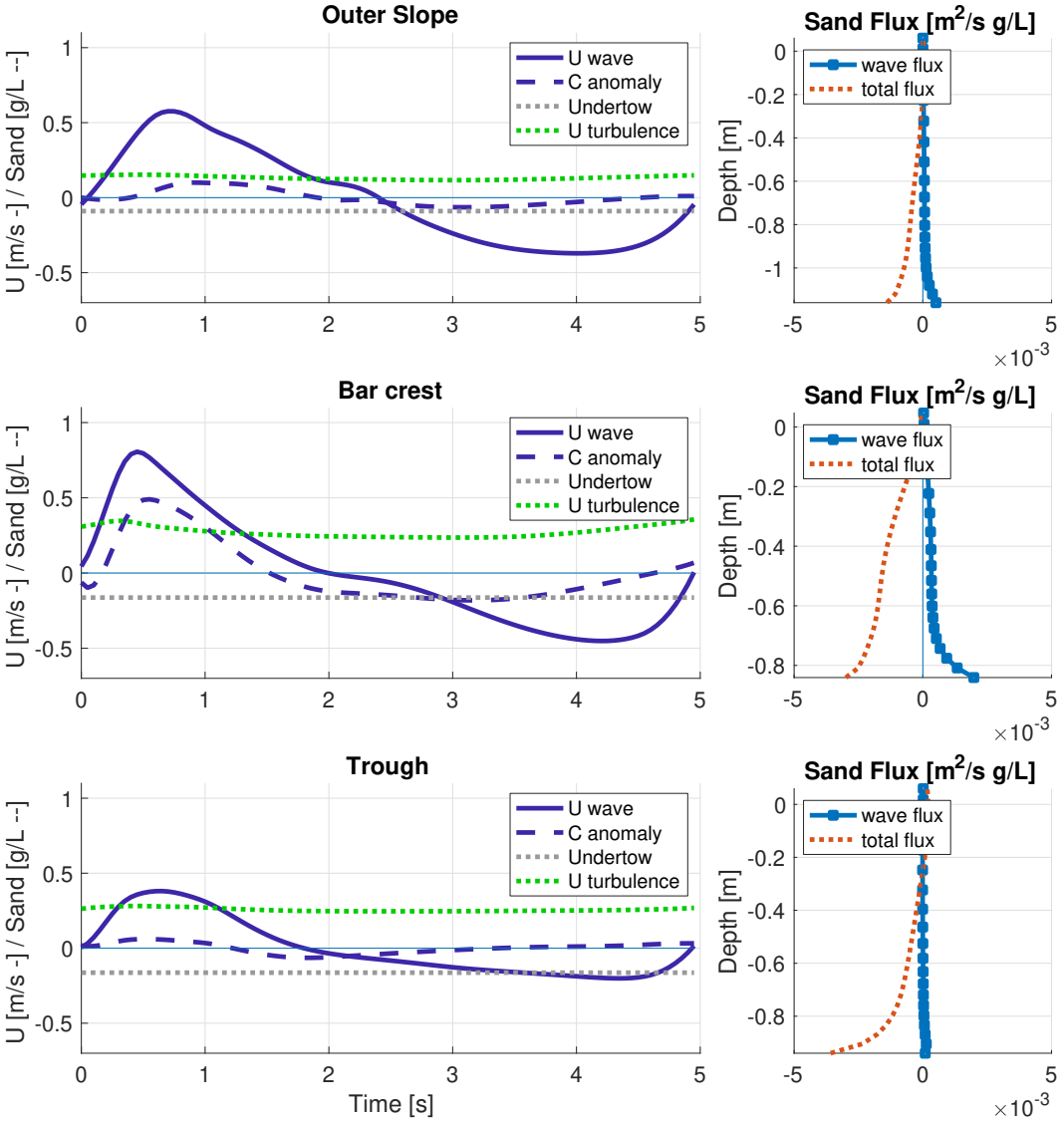

Figure 11: Same as Figure 10 but for the LIP-1B Flume experiment.

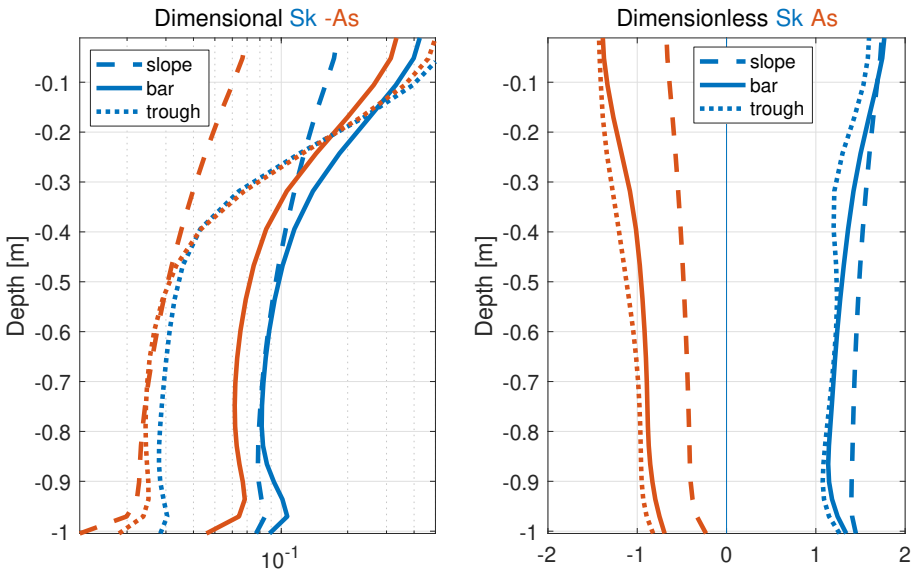

Figure 12: Ensemble-averaged analysis of wave asymmetry and skewness profiles (absolute and normalized) at three locations around the sandbar, during the accretive LIP-1C Flume experiment.

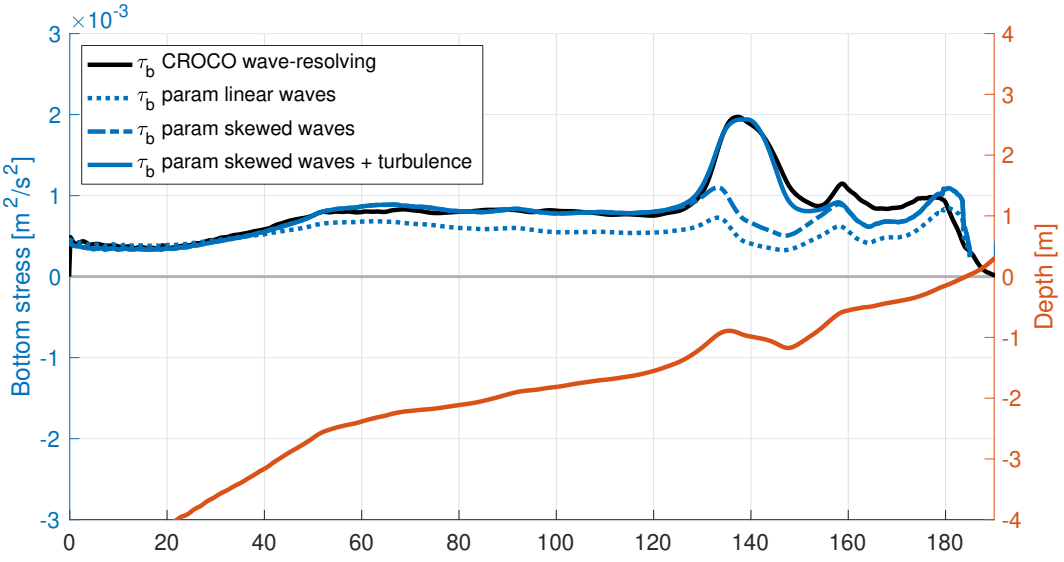

Figure 13: Bed shear stress profiles from the wave-resolving model and reconstructed from empirical formulations using wave-averaged values and linear wave theory with or without skewness correction.

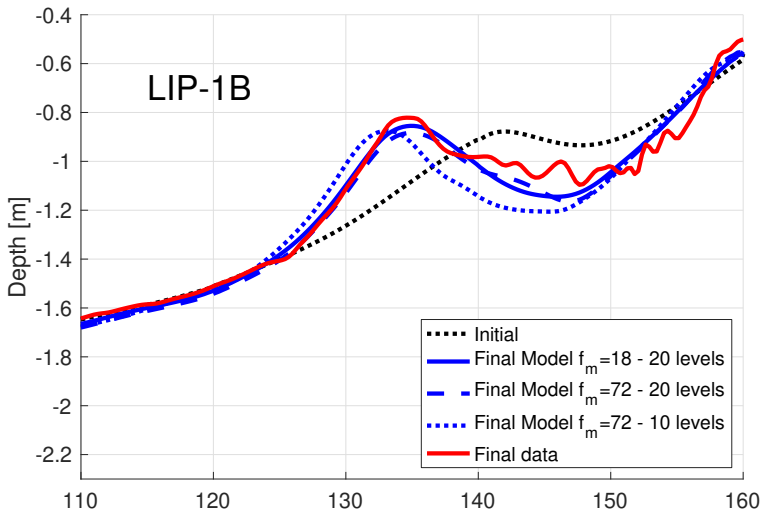

Figure 14: Model sensitivity to morphological acceleration parameter f_m and vertical grid resolution (number of vertical levels) during the erosion phase (LIP-1B).